ARTICLES
https://doi.org/10.1038/s41560-021-00782-0
nature energy

Check for updates

Reactive boride infusion stabilizes Ni-rich cathodes for lithium-ion batteries

Moonsu Yoon[1,4], Yanhao Dong[2,4], Jaeseong Hwang[1], Jaekyung Sung[1], Hyungyeon Cha[1], Kihong Ahn[1], Yimeng Huang[3], Seok Ju Kang[1], Ju Li[2,3]✉ and Jaephil Cho[1]✉

Engineered polycrystalline electrodes are critical to the cycling stability and safety of lithium-ion batteries, yet it is challenging to construct high-quality coatings at both the primary- and secondary-particle levels. Here we present a room-temperature synthesis route to achieve a full surface coverage of secondary particles and facile infusion into grain boundaries, and thus offer a complete 'coating-plus-infusion' strategy. Cobalt boride metallic glass was successfully applied to a Ni-rich layered cathode $LiNi_{0.8}Co_{0.1}Mn_{0.1}O_2$. It dramatically improved the rate capability and cycling stability, including under high-discharge-rate and elevated-temperature conditions and in pouch full-cells. The superior performance originates from a simultaneous suppression of the microstructural degradation of the intergranular cracking and of side reactions with the electrolyte. Atomistic simulations identified the critical role of strong selective interfacial bonding, which offers not only a large chemical driving force to ensure uniform reactive wetting and facile infusion, but also lowers the surface/interface oxygen activity, which contributes to the exceptional mechanical and electrochemical stabilities of the infused electrode.

A future energy infrastructure needs advanced cathode active materials for lithium-ion batteries (LIBs) with a higher energy and power density, longer cycle life and better safety than now available[1–3], but high-voltage and high-rate cycling often triggers accelerated degradation, premature failure and safety issues[4,5]. Much effort has been spent on exploring new cathode chemistry, introducing dopants into the bulk and at the surface, and designing nano-, micro- and/or heterostructures[6–9]. Coating is a widely exercised method to improve cathode stability, which can work synergistically with other cathode modifications[10–12]. Although a thin coating with a high stability and catalytic inertness is helpful, it is often difficult to achieve a 100% coverage in the synthesis due to a solid-on-solid wetting problem and the need to remain conformal during electrochemical cycling. These challenges set the motivation for the present work, which utilized a simple liquid–solution method to construct a high-quality cathode coating by reactive wetting with the oxide active material.

We chose a Ni-rich layered cathode $LiNi_{0.8}Co_{0.1}Mn_{0.1}O_2$ (NCM) of great industrial interest as a model system to demonstrate our coating strategy. During the electrochemical cycling of NCM, a series of detrimental processes take place, which include phase transformation in the bulk and at the surface[13], intergranular cracking of the secondary particles along grain boundaries (GBs)[14,15], the formation and growth of cathode electrolyte interphases (CEIs)[16] and side reactions that consume precious liquid organic electrolytes, generate gases and cause transition metal (TM) dissolution (which may later migrate and precipitate at the anode side and affect the anode stability)[17–19]. The above processes result in a continuous impedance growth and degrade the full-cell performance, especially under high-rate conditions. One key issue is the stability of surface oxygen, which becomes labile at high voltages and easily escapes. Such oxygen loss not only oxidizes organic electrolytes and evolves gases, but also leads to cation reduction and/or densification[20] and phase transformations[21,22], which may in turn initiate other degradation processes in a chain-reaction manner[23–25]. In this sense, it is beneficial to construct a coating that binds strongly with the surface oxygen to address the root cause of the high-voltage instability.

We selected a cobalt boride (Co_xB) coating with the following considerations:

1. Co_xB is a metallic compound that has no direct tie-lines with oxygen[26] and thermodynamically it would react with oxygen to form stable compounds, such as B_2O_3, Co_3O_4 and $Co_4B_6O_{13}$, which implies strong reactivity between Co_xB and the surface oxygen of NCM.
2. Co_xB has an exceptional oxidation resistance even at elevated temperatures (850–950 °C) (ref. [27]). This means that, even though Co_xB likes to react with oxygen, the reaction is kinetically self-limiting, probably due to the glass-forming ability of the B_2O_3-like product at the interface that forms a compact self-healing passivation layer[28,29]. Thus, although the reactive wetting ensures a complete coverage and tight adhesion between the Co_xB and NCM, it does not consume much oxygen from the NCM lattice and will probably maintain a metallic glass nature[30,31]. The passivation would kinetically suppress oxygen penetration and/or loss through this coating layer, and the interfacial polyanionic borate glass also incorporates the Li alkali metal that comes with NCM, which makes itself a mixed ionic and electronic conductor.
3. A Co_xB coating can be synthesized at room temperature[32,33], which eliminates the necessity of follow-up high-temperature treatments that may introduce additional complexity to the heavily optimized synthesis route of NCM.
4. Co_xB has been used to coat metal parts to improve their corrosion and wear resistance, and thus its mechanical properties should be good in the sense that it must not easily chip or fracture at the nanoscale.

[1]Department of Energy Engineering, School of Energy and Chemical Engineering, Ulsan National Institute of Science and Technology (UNIST), Ulsan, Republic of Korea. [2]Department of Nuclear Science and Engineering, Massachusetts Institute of Technology, Cambridge, MA, USA. [3]Department of Materials Science and Engineering, Massachusetts Institute of Technology, Cambridge, MA, USA. [4]These authors contributed equally: Moonsu Yoon, Yanhao Dong. ✉e-mail: liju@mit.edu; jpcho@unist.ac.kr

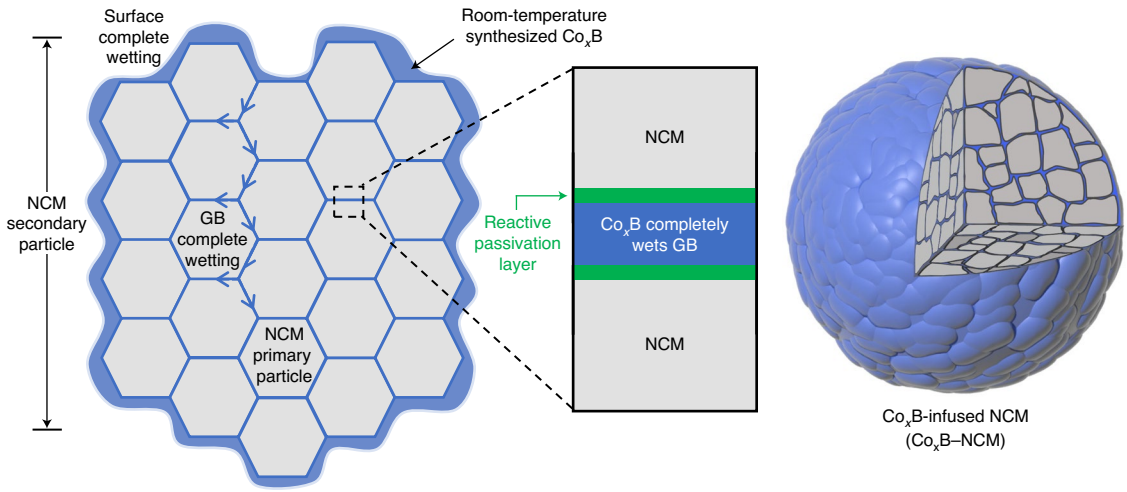

Fig. 1 | 'Coating-plus-infusion' microstructure for Co_xB-infused NCM. Schematic coating-plus-infusion microstructure in which Co_xB uniformly coats the surface of NCM secondary particle and infuses into GBs between the NCM primary particles.

Remarkably, we show that the as-synthesized Co_xB coating not only completely covered the surface of the NCM secondary particles, but also infused into the GBs between primary particles with a zero equilibrium wetting angle, which we abbreviate as 'infusion' to distinguish it from a typical surface coating. This is similar to the complete wetting of GBs by liquid metal (for example, liquid Ga in aluminium GBs), and intergranular amorphous nanofilms in ceramics. The infused microstructure (Fig. 1) dramatically improved the rate capability and cycling stability of NCM, including under high-discharge rate (up to 1,540 mA g^{-1}) and high-temperature (45 °C) conditions, as it greatly suppressed intergranular cracking, side reactions and impedance growth.

Co_xB fully covers NCM surface and infuses into GBs

Pristine NCM was synthesized by a co-precipitation technique, followed by calcination with lithium hydroxide in a flowing oxygen atmosphere. To obtain Co_xB–infused NCM (Co_xB–NCM), pristine NCM was added into the ethanol solution of $Co(NO_3)_2$, followed by the addition of an ethanol solution of $NaBH_4$ at room temperature under argon protection. Co_xB–NCM was then washed, collected and dried (Methods and Supplementary Fig. 1). Using inductive coupled plasma optical emission spectrometry (ICP-OES; Supplementary Table 1), we confirmed that the infused Co_xB has a composition close to $Co_{2.2}B$. Both pristine NCM and Co_xB–NCM have a layered structure as shown by the X-ray diffraction (XRD) data in Supplementary Fig. 2, with minimum Ni/Li cation mixing (1.2% for pristine NCM and 1.1% for Co_xB–NCM; Rietveld refinement data in Supplementary Table 2).

The synthesized NCM has a typical polycrystalline microstructure with spherical secondary particles (median diameter $D_{50} = 12$ µm; Supplementary Table 3), which consist of fine-grained primary particles (Fig. 2a). Such a microstructure is well maintained in Co_xB–NCM (Fig. 2b), in which a continuous uniform coating with a nanoscale fuzzy morphology was found at the surface under both scanning electron microscope (SEM, Fig. 2b; more examples in Supplementary Fig. 3) and transmission electron microscope (TEM, Fig. 2c,d; the fuzzy morphology has a mesoporous structure, as confirmed by the pore size distribution in Supplementary Fig. 4). We found that the coating layer at the surface of the crystalline NCM was amorphous and of thickness ~5 nm (Fig. 2c; coating layer identified by the contrast, as shown in Supplementary Fig. 5). From energy dispersive X-ray spectroscopy (EDS) mapping, it was enriched in Co and B and depleted in Ni and O compared with the NCM lattice (Fig. 2e), consistent with the targeted Co_xB composition. Remarkably, despite the room-temperature synthesis route and the lack of high-temperature annealing, Co_xB infused into the GBs between the NCM primary particles, as shown by the EDS mapping in Fig. 2f, and it completely wetted the GBs with an equivalent contact angle of zero degree. More examples of TEM-EDS mapping in Supplementary Figs. 6–8 confirmed the uniform surface coverage and infusion into the GBs deep inside the secondary particles up to >2–3 µm, which gave an unusually large room-temperature diffusivity of 1.4×10^{-16} to 3.1×10^{-16} m^2 s^{-1} for the Co_xB species as estimated with a two-dimensional (2D) random walk model. This thus indicates a huge driving force for 2D diffusion and/or penetration and supports a reactive wetting process, in which the coating layer spreads over the surface and GBs of the matrix driven by chemical reactions at the interface.

Benefiting from such reactive wetting, we found that Co_xB completely covered the surface of NCM, as supported by the X-ray photon spectroscopy (XPS) data in Fig. 2g–n (fitting details in Supplementary Table 4): compared to pristine NCM, Co_xB–NCM showed not only a strong B 1*s* signal around 187.8 eV (Fig. 2g, absent in pristine NCM in Fig. 2k)[32,34] and a negatively shifted Co $2p_{3/2}$ signal around 778.5 eV (Fig. 2h, versus 780.2 eV for the Co^{3+} $2p_{3/2}$ signal in pristine NCM in Fig. 2l; unlike Co^{3+} in NCM, Co_xB is metallic with Co peaks that shift towards a lower binding energy)[35], but also hugely suppressed Ni 2*p* and Mn 2*p* signals (Fig. 2i,j, versus strong signals in pristine NCM in Fig. 2m,n)[36]. As XPS is a surface-sensitive technique, the absence of Ni and Mn signals suggests a complete coverage of the Co_xB coating layer at the surface of NCM particles (so that the XPS signals were mainly contributed by the coating layer), with much better statistics than typical TEM characterizations.

Enhanced rate capability and cycling stability

We next investigated the electrochemical performance of pristine NCM and Co_xB–NCM as LIB cathodes in coin-type half cells under a high loading (10.5 ± 0.2 mg cm^{-2}, which corresponds to an areal capacity of ~2.05 mAh cm^{-2}) and a high electrode density (3.20 ± 0.03 g cm^{-3}). When first charged/discharged at 0.1*C* (1*C* defined as 220 mA g^{-1}) between 3.0 and 4.4 V versus Li/Li^+ at 25 °C, pristine NCM and Co_xB–NCM showed similar charge–discharge curves, a discharge capacity around 215 mAh g^{-1} and first-cycle Coulombic efficiency around 91.5%, and their redox behaviours were similar, as shown by a d*Q*/d*V* analysis (Supplementary Fig. 9a,b). However, Co_xB–NCM had a better

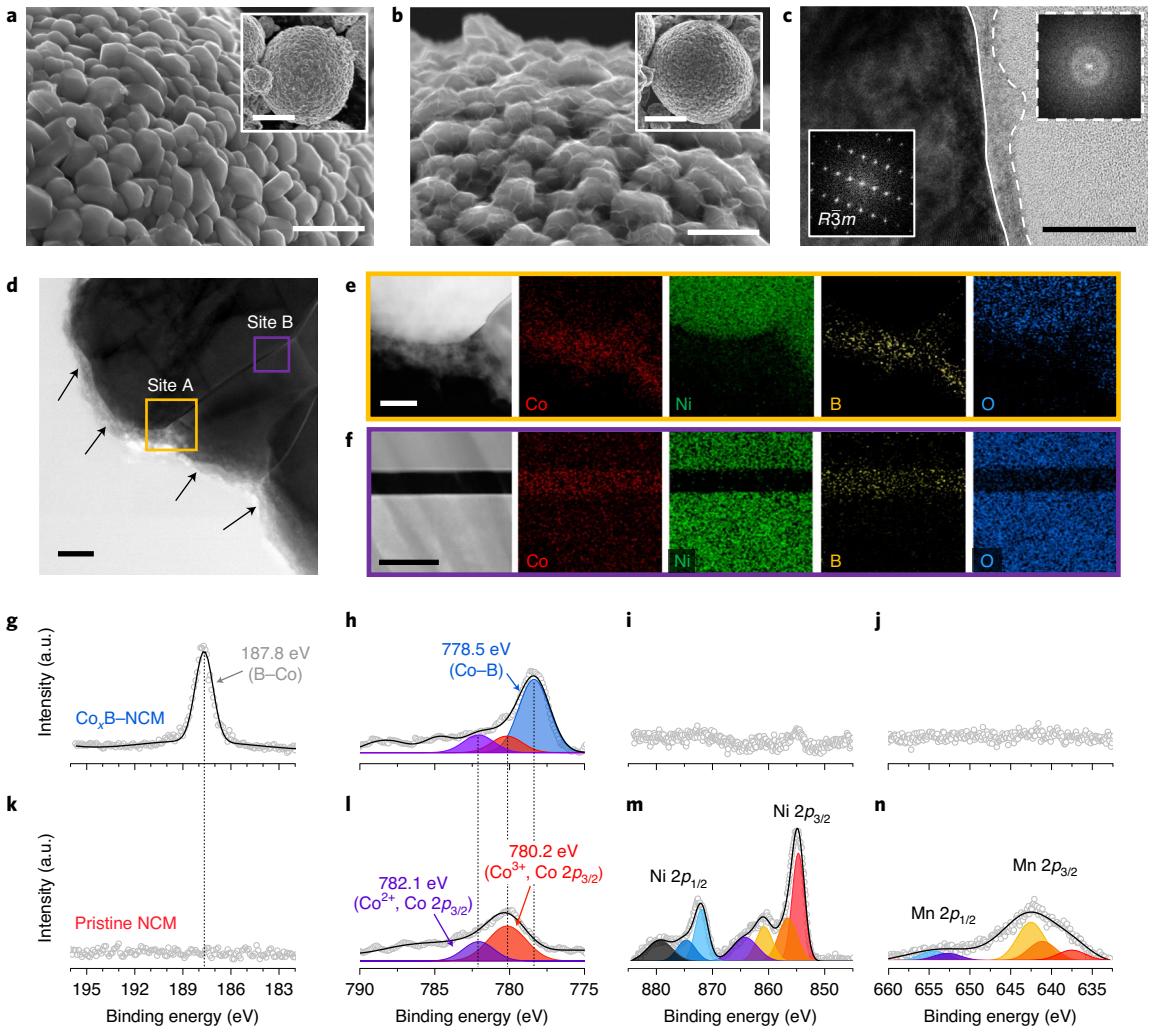

Fig. 2 | Uniform amorphous Co_xB infusion at the NCM surface and GBs. a,**b**, SEM images of pristine NCM (**a**) and Co_xB–NCM (**b**). Insets: lower-magnification SEM images showing the morphology of the NCM secondary particles. **c**,**d**, TEM images of cross-sectioned Co_xB–NCM near the surface. Insets of panel **c**: fast Fourier transform patterns showing crystalline NCM (bottom left) and amorphous Co_xB (top right). **e**, EDS mapping of site A in **d**. **f**, EDS mapping of site B in **d**. Scale bars, 1 µm (**a**,**b**), 5 µm (**a**,**b** insets), 20 nm (**c**,**e**,**f**), 50 nm (**d**). **g**–**j**, XPS spectra of B 1s (**g**), Co 2*p* (**h**), Ni 2*p* (**i**) and Mn 2*p* (**i**) for Co_xB–NCM. **k**–**n**, XPS spectra of B 1s (**k**), Co 2*p* (**l**), Ni 2*p* (**m**) and Mn 2*p* (**n**) for pristine NCM. Details for the XPS data analysis are listed in Supplementary Table 4. a.u., arbitrary units.

rate capability (Fig. 3a,b) and cycling stability (shown by the 1C cycling data performed after the rate tests in Fig. 3a and the 0.5 C cycling data in Supplementary Fig. 10). To gain a better understanding of the improved rate capability and cycling stability, we conducted a galvanostatic intermittent titration technique (GITT) measurements with a titration current of 0.5*C* after the first (41st cycle in the total number of cycling) and last (140th cycle in the total number of cycling) cycles of 1*C* cycling (Fig. 3a). As shown by the discharge profiles in Fig. 3c, a more severe polarization developed in cycled pristine NCM than in cycled Co_xB–NCM and the average voltage loss is 3.75 times larger in the former. The more detailed GITT analysis in Supplementary Fig. 11 demonstrates a minimum impedance growth in cycled Co_xB–NCM and a huge impedance growth in pristine NCM, mostly in the form of ohmic loss (which indicates degraded electron transport at the electrode level, which is consistent with observed intergranular cracking discussed below); this is further supported by electrochemical impedance spectroscopy (EIS) measurements (Supplementary Fig. 12).

To highlight the exceptional performance offered by Co_xB infusion, we tested under harsher conditions with a 7*C* discharge rate at 45 °C (note the cells were charged at 0.5*C* because the lithium metal anode (LMA) cannot afford such a fast charging rate). Although pristine NCM rapidly faded within 60 cycles, Co_xB–NCM could be stably cycled up to 200 cycles with a capacity retention of 82.2%, high Coulombic efficiency (Fig. 3d), high energy efficiency and stable average discharge voltage (Supplementary Fig. 13a–d). The rapid failure of pristine NCM in 7*C* discharge cycling is due to the kinetic reason of impedance overgrowth instead of a thermodynamic transformation, as the intermittent recovery step (conducted after every 100 cycles with a slow charge/discharge rate of 0.2*C*) can recover most of the capacity, as shown in Fig. 3d. The conclusion is further supported by EIS data measured after different 7*C* discharge cycles (Supplementary Fig. 14), which show a dramatic impedance growth of pristine NCM on cycling. Additional experiments were conducted with a 5*C* discharge rate at 45 °C (Supplementary Fig. 15), which again demonstrates the superior performance of Co_xB–NCM. Lastly, we tested pristine NCM and Co_xB–NCM in 400 mAh-pouch-type full-cells using a spherical graphite (Gr) anode and conducted long-term cycling in the range of 2.8–4.3 V at 25 °C. As shown in Fig. 3e, Co_xB–NCM has an impressive capacity retention of 95.0% (versus 79.2% for pristine

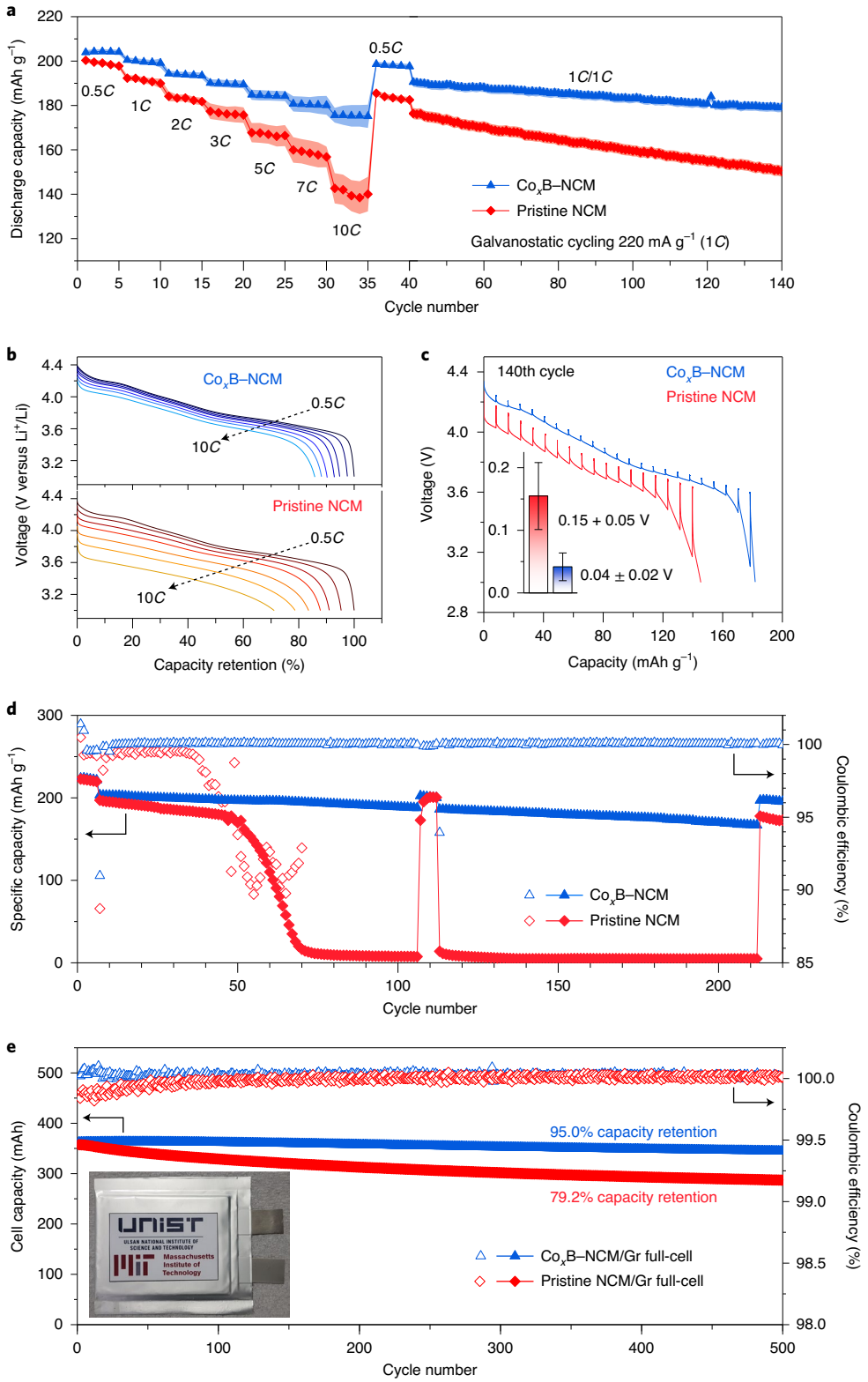

Fig. 3 | Superior electrochemical performance of Co_xB–NCM over pristine NCM. a, Rate tests and 1C cycling of Co_xB–NCM and pristine NCM in the range of 3.0–4.4 V versus Li/Li^+ at 25 °C. The shading shows the standard deviations calculated from five cells. **b**, Discharge curves at different rates for Co_xB–NCM (top) and pristine NCM (bottom). **c**, Discharge curves of the GITT measurements conducted after the 140th cycle in **a**. Inset: average voltage loss and its standard deviation (raw data available in Supplementary Fig. 11) over different GITT steps. **d**, 7C discharge cycling tests in the range of 3.0–4.4 V versus Li/Li^+ at 45 °C, with 6 intermittent cycles with 0.2C charge/discharges conducted after every 100 cycles. **e**, Cycling performance of Co_xB–NCM/Gr and pristine NCM/Gr full-cells at 1.0C in the range of 2.8–4.3 V at 25 °C. Inset: photo of an assembled pouch cell.

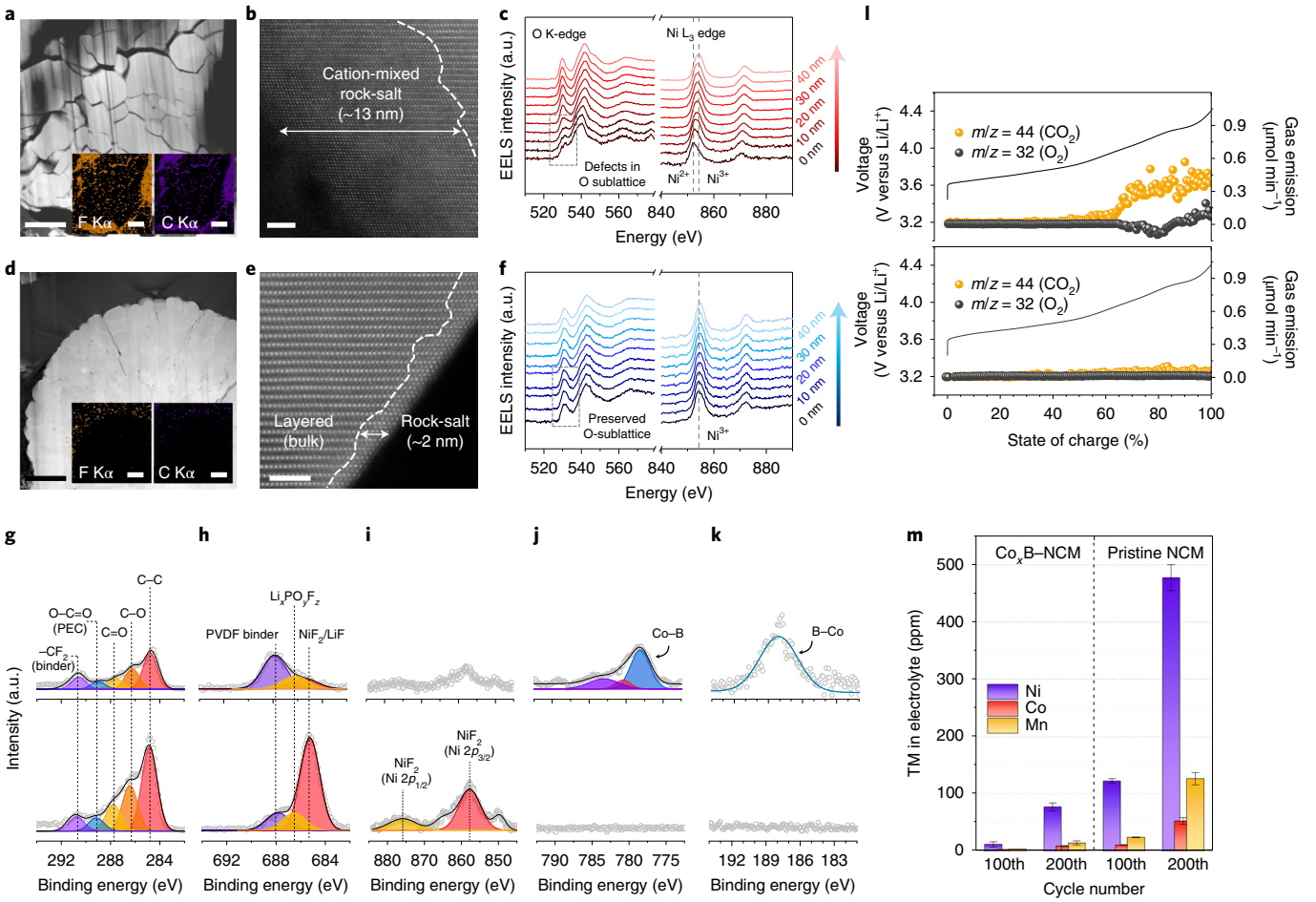

Fig. 4 | Co_xB infusion simultaneously suppresses microstructural degradation and side reactions. a, TEM image and EDS mapping (inset) of pristine NCM after 200 cycles under a 7*C* discharge rate at 45 °C. **b**,**c**, High-resolution transmission electron microscopy (HR-TEM) at a fresh surface generated by intergranular cracking (**b**) and an EELS line scan at a secondary-particle surface in cycled pristine NCM (**c**). **d**, TEM image and EDS mapping (inset) of Co_xB-NCM after 200 cycles under a 7*C* discharge rate at 45 °C. **e**,**f**, HR-TEM (**e**) and EELS line scan (**f**) at a secondary-particle surface in cycled Co_xB-NCM. Scale bars, 2 μm (**a**,**d**), 2 nm (**b**,**e**). **g**–**k**, XPS spectra of C 1s (**g**), F 1s (**h**), Ni 2*p* (**i**), Co 2*p* (**j**) and B 1s (**k**) for Co_xB-NCM (top) and pristine NCM (bottom) after 200 cycles under a 7*C* discharge rate at 45 °C. PEC, poly(ethylene carbonate); PVDF, poly(vinylidene fluoride). **l**, In situ DEMS data of pristine NCM (top) and Co_xB-NCM (bottom) during first charge at 0.2*C* in the voltage range 3.0–4.4 V versus Li/Li^+ at 25 °C. **m**, Dissolved Ni, Co and Mn in the electrolytes measured by ICP-OES after 100 and 200 cycles under a 7*C* discharge rate at 45 °C (electrolytes from three different cells were measured to obtain the averages and standard deviations for each data point).

NCM) and a high Coulombic efficiency at 1.0*C*/1.0*C* charge/discharge for 500 cycles (more detailed electrochemical performances are given in Supplementary Fig. 16). Therefore, Co_xB infusion can greatly enhance the rate capability and cycling stability of NCM with a suppressed impedance growth and voltage loss, especially under high-rate and high-temperature conditions.

Mitigating microstructural degradation and side reactions

Pristine NCM and Co_xB–NCM show dramatically different microstructures after cycling. After 200 cycles under a 7*C* discharge rate at 45 °C, we observed severe intergranular cracking in pristine NCM, as shown by TEM (Fig. 4a) and SEM (Supplementary Fig. 17a,b), which created more electrolyte-exposing fresh surfaces and led to extensive CEI formation, as indicated by the EDS mapping of F and C both at the surface and inside the secondary particle (insets of Fig. 4a). In comparison, the secondary particles of Co_xB–NCM remained intact without cracking, as confirmed by TEM (Fig. 4d) and SEM (Supplementary Fig. 17c,d), and the F and C signals were weaker (insets of Fig. 4d), which suggests less electrolyte infiltration and CEI formation[37]. Similarly, suppressed cracking by Co_xB infusion was also observed in the initially charged cathodes as well as in those after 500 cycles in pouch cells (Supplementary Figs. 18 and 19). The contrasting cracking behaviours are interesting because intergranular cracking of Ni-rich cathodes is typically attributed to anisotropic lattice expansion and/or shrinkage and heterogeneous charge/discharge kinetics during electrochemical cycling[38,39], which can hardly be removed by cathode coating. Indeed, as shown by in situ XRD during electrochemical cycling (Supplementary Figs. 20 and 21), pristine NCM and Co_xB–NCM undergo the same bulk phase transformation and lattice expansion and/or shrinkage (Supplementary Fig. 22). Similar observations were also recently reported in the literature, in which the appropriate cathode coatings and electrolyte compositions can efficiently reduce intergranular cracking[11,40,41]. Therefore, large-scale cracking cannot be solely driven by mechanical stress and/or strain alone; instead, it should also involve chemical side reactions at the GBs, in other words, a stress corrosion cracking (SCC) problem.

The hypothesis is supported by simultaneously suppressed side reactions and surface phase transformations by Co_xB infusion. To demonstrate the correlation, we first characterized the fresh surface

generated by intergranular cracking in cycled pristine NCM under TEM (Fig. 4b), which showed a thick (~13 nm) cation-mixed rock-salt phase (which originated from surface oxygen loss followed by surface cation densification). From electron energy loss spectroscopy (EELS) measurements in Fig. 4c and Supplementary Fig. 23a, we found severe TM reduction (Ni^{3+} reduced to Ni^{2+} shown by the Ni L_3 edge) and defects in the oxygen sublattice (shown by the O K edge) near the surface of cycled pristine NCM[42,43]. In comparison, for cycled Co_xB–NCM, we found a thinner transformed cation-mixed rock-salt phase (~2 nm, Fig. 4e) even at the surface of the secondary particles and much less Ni reduction and oxygen defects (Fig. 4f). The suppressed surface cation reduction, cation densification and surface phase transformation apparently benefit from Co_xB infusion, as the morphology and chemistry remained unchanged at both surfaces and GBs, confirmed by TEM (Supplementary Figs. 23b, 24 and 25a) and EDS (Supplementary Figs. 24d and 25b).

Second, the surfaces of cycled samples were characterized by XPS, in which the signals of C 1*s* (contributed by organic CEI components, such as polycarbonates and semicarbonates)[41,44,45], F 1*s* (contributed by CEI components of metal fluorides, such as NiF_2 and LiF) and Ni 2*p* signals (contributed by Ni-containing CEI components, such as NiF_2) (ref. [46]) were observed in cycled pristine NCM were stronger than those in cycled Co_xB–NCM (Fig. 4g–i; see detailed discussions in Supplementary Table 5). Meanwhile, strong Co 2*p* and B 1*s* signals were observed in cycled Co_xB–NCM, which indicates the Co_xB surface coating was not covered by thick CEIs, even after prolonged cycling. Both observations above suggest a suppressed CEI growth in Co_xB–NCM (Fig. 4j,k).

Third, by in situ differential electrochemical mass spectrometry (DEMS) measurements (Fig. 4l), we found much less gas evolution (CO_2 and O_2) during the first charge cycle of Co_xB–NCM than during that of pristine NCM. This suggests that Co_xB infusion effectively lowered the surface and GB oxygen activity and suppressed the electrolyte oxidation (the Co_xB infusion may also work by physically separating the electrolyte from cathode surface). Meanwhile, from ICP-OES measurements of the electrolytes in cycled cells (Fig. 4m and Supplementary Table 6), we found less TM dissolution (Ni, Co and Mn) in cycled Co_xB–NCM than in pristine NCM. Therefore, we conclude that our coating efficiently mitigated the side reactions between the cathode and electrolyte, as well as side-reaction products in the solid (CEIs), gas (CO_2 and O_2) and soluble (dissolved Ni, Co and Mn) forms, and the suppressed side reaction correlated well with the eliminated microstructural degradation, which supports the proposed mechanism of SCC retardation.

Lastly, the boride infusion treatment improved safety, as demonstrated by differential scanning calorimetry (Supplementary Fig. 26). The exothermal reaction in Co_xB–NCM charged at 4.4 V (versus Li/Li^+) took place at a higher temperature of 269.5 °C with a lower heat generation of 487.9 J g^{-1} compared with 250.9 °C and 786.3 J g^{-1}, respectively, for 4.4-V-charged pristine NCM. This is strong proof of the chemical passivation kinetics we postulated, as oxygen release during cathode thermal decomposition is an important step in the exothermic reaction chain, and by reducing oxygen release, Co_xB–NCM is able to delay the thermal runaway and reduce the total heat released[47].

Crossover effect on LMA

High-energy-density lithium metal batteries are currently under development[48] and we found that the dissolved TMs from the NCM cathode greatly affected the morphology and electrochemical performance of the LMA during the 7*C* discharge cycling at 45 °C. After 200 cycles, we found that the surface of the LMA paired with pristine NCM became rough (Fig. 5a) with a porous layer that consisted of mossy lithium and solid–electrolyte interphases (SEIs), as shown in Fig. 5b. EDS mapping of the porous layer in Fig. 5c identified not only non-uniform C and F distributions, but also strong Ni signals enriched at the SEI/LMA interface, from the crossover effect of Ni dissolution, migration and deposition on the anode[10,19]. In comparison, the LMA paired with Co_xB–NCM had a smooth surface and a dense SEI layer (Fig. 5d,e). The contrasting morphology was closely related to the composition and stability of the SEI, and by XPS measurements (Fig. 5f) we confirmed the SEI of the LMAs paired with Co_xB–NCM indeed had much weaker Ni signals than those paired with pristine NCM. (Note that Mn and Co were undetectable, as shown by the XPS in Supplementary Fig. 27 for cycled LMAs paired with both pristine NCM and Co_xB–NCM, probably due to lower dissolved concentrations in the electrolytes.) Electrochemically, the deposited Ni-induced morphological instability would degrade the performance of the LMA, which was proved by the cycling experiments of Li/Li symmetric cells (Supplementary Fig. 28). Therefore, the suppressed TM dissolution by our coating conveyed an additional benefit by removing the crossover effect on the LMA and improved the full-cell cycling stability (Supplementary Fig. 29).

Selective interfacial bonding and suppressed oxygen activity

For the atomistic details, first-principles calculations were conducted on the (104) surface of $LiNiO_2$ and on the interface between the $LiNiO_2$ (104) surface and amorphous Co_xB. As shown by the relaxed atomic structure of a $LiNiO_2$ slab with the top and bottom (104) surfaces in Supplementary Fig. 30a, the LiO_6 (grey) and NiO_6 (purple) octahedra were truncated at the surfaces, which created underbonded surface oxygen with two kinds of local structures: type I coordinated by two Ni and three Li, and type II coordinated by three Ni and two Li. Note that in the bulk of $LiNiO_2$, the lattice oxygen was always coordinated by three Ni and three Li (inset of Supplementary Fig. 30b), which promoted a strong hybridization between the Ni 3*d* and O 2*p* orbitals (with three Ni–O–Li local configurations) and lowered the energy level of the occupied O 2*p* states (Supplementary Fig. 30b). However, the type I surface oxygen had one nil–O–Li configuration (in addition to two Ni–O–Li configurations; inset of Supplementary Fig. 30c), which indicates a weaker Ni 3*d*–O 2*p* hybridization, and creates more high-energy O 2*p* states close to the Fermi level E_F (Supplementary Fig. 30c). This is the origin of the surface oxygen instability, which is prone to lose electrons at high voltages and subsequently evolves oxygen gas. Indeed, similar analyses were put forward for Li-rich cathode materials[49,50], in which the Li–O–Li local configuration raises the electronic energy of O 2*p* states and is responsible for the observed oxygen redox.

At the interface between $LiNiO_2$(104) surface and amorphous Co_xB (Fig. 6a), Co and B preferentially bond with the surface O of $LiNiO_2$, but not with Li or Ni. The interfacial Co–O and B–O bonds are stronger than the lattice Ni–O bond, as indicated by the stronger electron cloud sharing for the former in the charge density plot (Fig. 6b,c). Note that in Fig. 6c, the B–O bond has a short bond distance (1.33 Å) and the electron cloud of O polarizes towards B, which suggests a covalent bonding nature. Considering the local structure, the type I 'surface' O (now becoming an interfacial O) is coordinated either by one Co, two Ni and three Li atoms (inset of Fig. 6e) or by one B, two Ni and three Li atoms (inset of Fig. 6f; the strong B–O bond pulls O away from the centre of the original 'octahedral' site and the polyhedron becomes similar to a distorted square pyramid). Even though the O coordination (Fig. 6e) is similar to that in the lattice (by three Ni and three Li atoms, inset of Fig. 6d), the strong Co–O bond effectively lowers the energy of the O 2*p* states (Fig. 6e), which have less high-energy states close to E_F than that of the lattice O (Fig. 6d). A more dramatic energy-level lowering is achieved by the strong covalent B–O bond, as shown in Fig. 6f, which greatly stabilizes the interface O. We further verified that such an analysis approach on local structures is robust, as the same conclusion can be drawn from the amorphous Co_xB GB

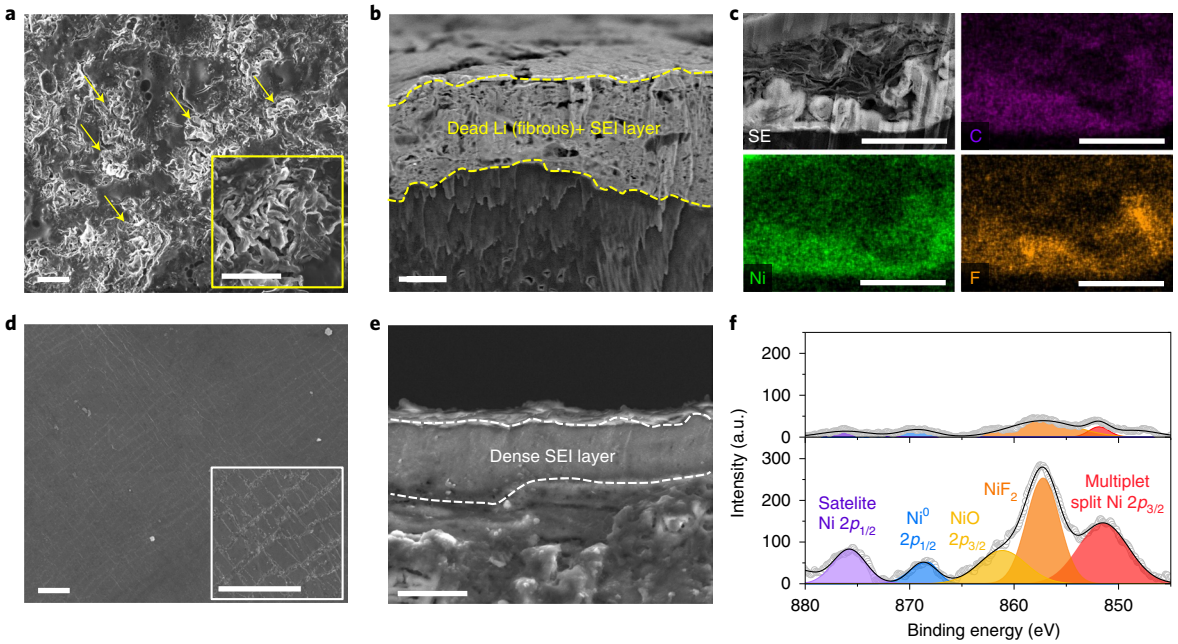

Fig. 5 | Morphology and chemical characteristics of cycled LMA. a–**c**, Top-view (**a**) and cross-sectional (**b**) SEM images, and EDS mapping (**c**) of LMA paired with pristine NCM after 200 cycles under a 7*C* discharge rate at 45 °C. **d**,**e**, Top-view (**d**) and cross-sectional (**e**) SEM images of LMA paired with Co_xB-NCM after 200 cycles under a 7*C* discharge rate at 45 °C. Scale bars, 20 μm (**a**,**d**), 5 μm (**b**,**c**,**e**). **f**, XPS spectra of Ni 2*p* for Co_xB-NCM (top) and pristine NCM (bottom) after 200 cycles under a 7*C* discharge rate at 45 °C.

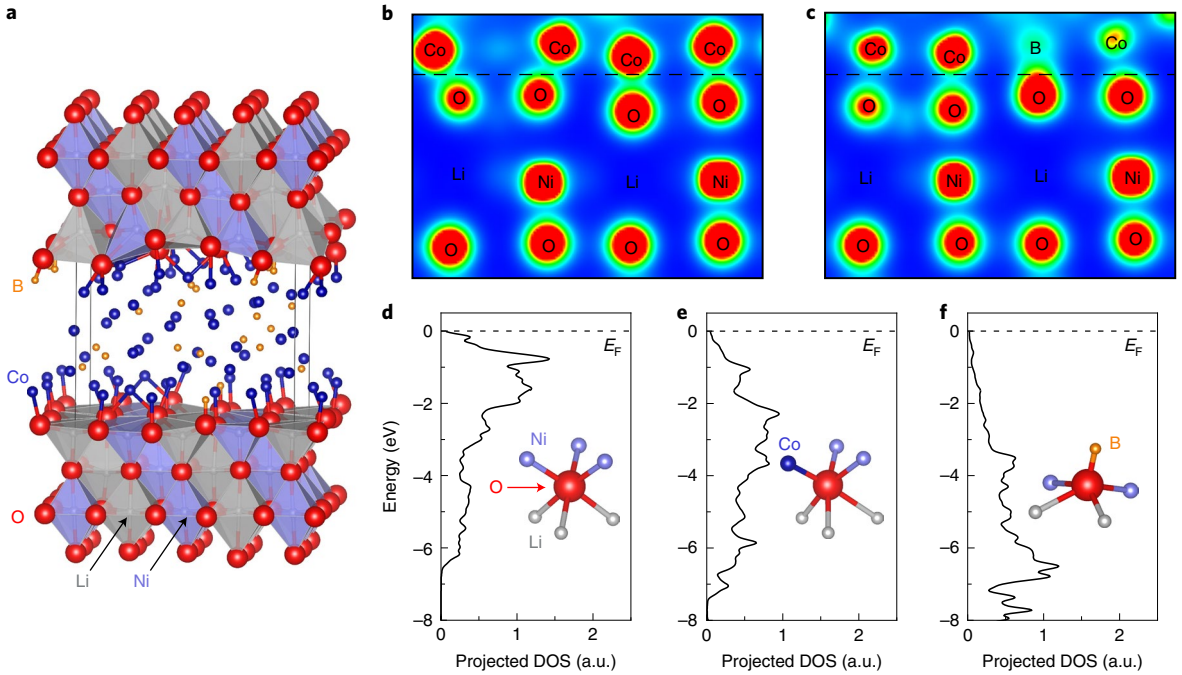

Fig. 6 | Strong interfacial bonding suppresses oxygen activity. a–**c**, Atomic structure (**a**) and 2D slices of the charge density distribution of a simulated interface between the $LiNiO_2$(104) surface and amorphous Co_xB across 4 Co–O bonds (**b**) and 3 Co–O and 1 B–O bond (**c**) (dashed lines denote the Co_xB/$LiNiO_2$ interface). **d**–**f**, Projected density of states (DOS) and schematic local environment (**d**–**f** insets) of lattice oxygen coordinated by three Ni and three Li atoms (**d**), interface oxygen coordinated by one Co, two Ni and three Li atoms (**e**) and interface oxygen coordinated by one B, two Ni and two Ni atoms (**f**).

phases with different atomic structures (Supplementary Fig. 31). The above results clearly demonstrate that the chemical nature of reactive wetting is the selective Co–O and B–O bonds formed at Co_xB/NCM interface, and the superior stability has an electronic-structure origin that effectively suppresses interface oxygen activity. This rationalizes the design of a reactive-wetting metal–metalloid glass[30,31] coating materials with selective bonding, which ensures not only a uniform complete coverage but also stabilizes the surface oxygen.

Regarding the improved mechanical stability, although Co_xB infusion mitigates SCC by stabilizing surface oxygen and suppressing the side reactions, it also benefits from a mechanical perspective, as less cracking was found even at the end of the first charge (Supplementary Fig. 18) when the chemical effect should be less conspicuous. Consistent with the strong interfacial bonds and reactive wetting, we found a 4.6 times higher 'opening' strength (41 GPa; Supplementary Fig. 32) in first-principles cohesive zone calculations at the Co_xB/$LiNiO_2$ interface compared with that of bulk $LiNiO_2$ (9 GPa), which would help to suppress a Mode I crack. For Mode II and III cracks, we suspect that the metallic glass Co_xB phase is shear weak and can assist inelastic grain-boundary sliding via bond switching that preserves the coordination number. This could be an effective way to release strain energy and avoid stress concentration at the GBs, and thus benefit the long-term mechanical integrity (Supplementary Fig. 19). The above picture allows us to propose design principles for reactive coating/infusion. For oxide cathodes that are synthesized under an oxidizing atmosphere, a reducing agent (an electron donor) has a strong affinity to surface oxygen. This applies to metallic compounds, especially borides, phosphides, silicides and so on, which can form strong covalent bonds with surface oxygen, in other words, create interfacial polyanion groups that stabilize the labile surface oxygen. The latter concept applied to the 3D lattice is exactly the one that led to the invention of polyanion LIB cathodes (for example, $LiFePO_4$) that have excellent stability and safety. Meanwhile, for the reactive wetting process to happen, such covalent bonds should be formed in situ at the interface and not pre-exist in the coating materials so that a large driving force can be derived from the interfacial chemical reactions. This means that borides reactively wet oxide particles, but borates cannot[51]. Regarding the synthesis route of the coating material, this may require a highly reducing condition, as in the work presented here in which $NaBH_4$ was used. To minimize the TM reduction at the interface (when NCM is treated with $NaBH_4$, a slight reduction of Ni but not of Co and Mn may occur at the surface, as shown in Supplementary Fig. 33), a low synthesis temperature is thus preferable, such as room temperature. Such a TM reduction definitely must not happen in the bulk.

Conclusions

To summarize, we have demonstrated a simple method to construct a high-quality Co_xB metallic glass infusion (beyond that of typical surface coating) of NCM secondary particles by reactive wetting. Under the strong driving force of an interfacial chemical reaction, nanoscale Co_xB metallic glass not only completely wraps around the secondary particle surfaces, but also infuses into the GBs between primary particles. This is extraordinary given that it happens at room temperature, and the secondary particle does not alter the crystalline bulk, but produces drastic changes in the GBs as they are infiltrated by reactive wetting. Consequently, it offers a superior electrochemical performance (especially a high-rate cycling stability at 7*C*, a high-temperature cycling at 45 °C and an impressive 95.0% capacity retention over 500 cycles in practical pouch-type full-cells) and better safety by mitigating the entwined cathode-side intergranular SCC, microstructural degradation and side reactions, as well as the TM crossover effect to the anode. Mechanistically, our atomistic simulations revealed a strong, selective interfacial bonding between Co_xB and NCM, which provides a consistent explanation of the reactive wetting and suppressed oxygen activity observed experimentally. The reactive infusion of oxides by other TM boride, phosphide and/or silicide metallic glasses, to produce 'functional cermets', should be a generic modification strategy for many electrodes used in advanced energy storage and conversion.

Methods

Synthesis. Hydroxide precursors of NCM were synthesized by a co-precipitation method. An aqueous solution that contained 3.2 M Ni^{2+}, 0.4 M Co^{2+} and 0.4 M Mn^{2+} was prepared by dissolving $NiSO_4{\cdot}6H_2O$, $CoSO_4{\cdot}7H_2O$ and $MnSO_4{\cdot}6H_2O$ with a molar ratio of 8:1:1. It was continuously fed into a stirred tank reactor (capacity of 4 l) with 4.0 M NaOH and 0.4 M NH_4OH solutions under feeding rates of 300, 300 and 40 ml h^{-1}, respectively. A reaction temperature of 50 °C was stably maintained by external water circulator for 20 h, after which the hydroxide precursors were washed, collected and dried at 110 °C for 12 h. NCM was then synthesized by mixing the hydroxide precursors (composition treated as $(Ni_{0.8}Co_{0.1}Mn_{0.1})(OH)_2$) with $LiOH{\cdot}H_2O$ in a molar ratio of 1:1.025, followed by a heat treatment at 450 °C for 2 h and then at 800 °C for 10 h in flowing oxygen. To coat and infuse NCM with the Co_xB compound, 100 ml of anhydrous ethanol solution that contained 0.009 M $Co(NO_3)_2{\cdot}6H_2O$ was first prepared under vacuum with a Schlenk line to remove the dissolved oxygen. NCM powders (5.0 g) were next added under vigorous stirring and under argon protection. Subsequently, 2 ml of ethanol solution that contained 0.078 M $NaBH_4$ was gradually added and maintained for 2 h under vigorous stirring and under argon protection. The samples were then washed with anhydrous ethanol, collected by vacuum filtration and dried at 120 °C under vacuum overnight.

Material characterizations. The chemical compositions of the cathode material and electrolyte were determined by an ICP-OES (Varian 700-ES, Varian, Inc.). Phases and crystallographic structures were characterized by XRD using a parallel-beam XRD instrument (Smartlab, Rigaku, with Cu Kα of wavelength 1.542 Å). Specific surface areas were measured by a surface area and porosity analyser (TriStar II, Micromeritics) based on Brunauer–Emmett–Teller theory. The water content was measured three times for each sample using Karl-Fischer coulometric titration (Metrohm 831 KF Coulometer) and are listed in Supplementary Table 7. Impurity content (LiOH and Li_2CO_3) amounts were measured by an acid-based titration method[52] (Mettler Toledo Titrator) and are listed in Supplementary Table 8. Briefly, 10 g of cathode powders were soaked into 100 ml of deionized water. After stirring for 15 min, 40 ml of clear solution was separated by vacuum filtering and additional 100 ml of deionized water was added. A flow of 0.1 M HCl was added to the solution under stirring, while the pH of the solution was recorded. The experiments were considered finished when the pH of the solution reached 4.0. In situ XRD measurements were conducted on cathodes assembled with a battery cell kit (Rigaku) in a glove box. After installing the assembled battery cell kit on an XRD stage, the cells were first cycled at 0.1*C* between 3.0 and 4.4 V versus Li/Li^+ as a formation step, after which in situ XRD measurements were performed with Cu Kα radiation (Smartlab, Rigaku) during the charge process at a rate of 0.05*C* between 3.0~4.4 V versus Li/Li^+. Cross-sections of the cathodes and LMAs were cut by ion milling (IM-40000, Hitachi) and characterized under a SEM (Verios 460, FEI) equipped with an EDS (XFlash 6130, Bruker) detector. The morphologies and chemical compositions of the prepared cathode powders and electrodes were also characterized by SEM and EDS. The surface chemistry was analysed by XPS (Thermo Scientific Kα spectrometer). Before the XPS measurements, all the samples were rinsed by a dimethyl carbonate (DMC) solvent to remove the residual electrolyte salt and by-products. In situ DEMS measurements were conducted on Swagelok type cells between 3.0 and 4.4 V (versus Li/Li^+); the details are described elsewhere[53]. For the TEM analysis, samples were prepared by dual-beam focused ion beam (FIB, Helios 450HP, FEI) using a 2–30 kV Ga ion beam. Prior to the analysis in the FIB workstation, epoxy soaking and carbon deposition were conducted to avoid damage to the Ga ion beam and preserve the sample morphology in subsequent lift-out and thinning processes. After lift-out, the prepared TEM samples were thinned to 200 nm using a 30 kV Ga ion beam. The thinned samples were next polished to remove surface contamination using an Ar-ion milling system (Model 1040 Nanomill, Fischione) and immediately transferred and inspected under TEM. HR-TEM (ARM300, JEOL) was conducted at 150 and 300 keV to collect scanning transmission electron microscopy images for the atomic and structural analysis. For the elemental and spectrum analysis, EELS and EDS were conducted by HR-TEM (Aztec, Oxford Instruments). The thermal stability of charged cathodes was evaluated by differential scanning calorimeter (STAR 1, Mettler Toledo). The cathodes were first charged to 4.4 V (versus Li/Li^+) at 0.1*C* and then held at 4.4 V for an additional 2 h. The cathode materials were next collected from disassembled cells, rinsed with DMC to remove residual electrolytes and dried. Charged cathode powders (5.0 mg) were placed in a hermetic aluminium pan with 3 µl of electrolyte. During the differential scanning calorimetry measurements, the temperature was increased from the ambient condition to 400 °C at a constant heating rate of 10 °C min^{-1}.

Electrochemical measurements. Composite cathodes were prepared by mixing 90 wt% active material, 5 wt% Super-P (as the conductive agent) and 5 wt% poly(vinylidene fluoride) (as the binder) in *N*-methyl-2-pyrrolidone. The slurry obtained was coated onto aluminium foil and dried at 120 °C for 2 h. All the cathodes for the coin-type half cells were controlled with a loading level of 10.5 ± 0.2 mg cm^{-2} (measured over five punched electrodes) and an electrode density of 3.20 ± 0.03 g cm^{-3} (measured over five punched electrodes). Lithium metal batteries were assembled using 2032 R coin-type cells in an argon glove box, with the cathodes (diameter 14 mm) and lithium metal foils (diameter 15 mm) as the counter and reference electrode, respectively, and 1.15 M $LiPF_6$

in ethylene carbonate (EC)/ethyl methyl carbonate (EMC)/DMC with 5 wt% fluoroethylene carbonate (EC:EMC:DMC = 3/4/3 vol%; Panax Starlyte) as the electrolyte (0.2 g added to each coin cell). All the coin cells were evaluated in a constant current–constant voltage mode between 3.0 and 4.4 V (versus Li/Li^+) at 25 and 45 °C. For all the coin cells, the first charge–discharge cycle was conducted at 0.1*C*. Here 1.0*C* is defined as 220 mA g^{-1}. To evaluate the rate capability, the cells were charged at 0.5*C* and discharged at rates of 0.5, 1.0, 2.0, 3.0, 5.0, 7.0 and 10.0*C*. After the rate testing, the cells were charged/discharged at 1.0 C in the constant current–constant voltage (0.05 C cutoff) mode for another 100 cycles (41st to 140th cycles in the total number of cycles) to evaluate the cycling stability between 3.0 and 4.4 V (versus Li/Li^+) at 25 °C. GITT measurements were then conducted after the first and last cycles (41st and 140th cycle in the total number of cycles, respectively) of 1.0*C* cycling between 3.0 and 4.4 V (versus Li/Li^+) with a titration step at 0.5*C* of 8 min and a relaxation step of 1 h. To evaluate the high-rate cycling stability, the cells were charged at 0.5*C* and discharged at 5.0/7.0*C*. After every 100 cycles, an intermittent recovery step with charge/discharge rate of 0.2*C* was conducted for six cycles. EIS measurements were conducted on cells charged to 4.4 V (versus Li/Li^+) from 1 to 10 MHz and with an a.c. voltage amplitude of 10 mV using a VMP-300 potentiostat (Bio-logic). Nickel-containing electrolytes were prepared by dissolving 0, 200 and 600 ppm $Ni(TFSI)_2$ (TFSI, trifluoromethylsulfonimide) in the base electrolyte (1.15 M $LiPF_6$ in EC:EMC:DMC = 3/4/3 vol%). Li/Li symmetric cells were assembled in the glove box with 80 µl of the prepared electrolyte for each cell. Galvanostatic cycling was performed on a symmetric Li/Li cell at a Li plating/stripping current density of 1.0 or 2.0 mA cm^{-2} with a cycling capacity of 2.0 mAh cm^{-2} (2 h for each step). For full-cell tests, pristine NCM and Co_xB–NCM cathodes and Gr anodes were utilized to assemble 400-mAh-scale pouch-type full-cells. The ratio of negative to positive electrode capacity (N/P ratio) was fixed at 1.11 ± 0.01. The cathode loading level was 13.5 mg cm^{-2} on each side of the double-side coated Al foil. The anode loading level was 8.2 mg cm^{-2} on each side of the double-side coated Cu foil. The graphite electrode density was 1.44 g cm^{-3} and the cathode density was 3.35 g cm^{-3}. The pouch-type full-cells were assembled in a dry room with a humidity of less than 1%. The separator and liquid electrolytes were the same as those used in coin cells. The weight of the electrolyte used in full-cells was 1.0 g, which corresponded to 2.5 g Ah^{-1}. The cycling voltage window was at 2.8–4.3 V, and a two-formation cycle was conducted at 0.1*C* before long-term cycling of 500 cycles at 1*C*. Details for full-cell specifications are also listed in Supplementary Table 9. All the electrochemical tests (except for EIS) were carried out using a TOSCAT-3100 battery cycler (TOYO SYSTEM).

Simulations. Spin-polarized first-principles calculations were conducted using the Vienna ab initio simulation package based on density functional theory (DFT) using the projector augmented-wave method with the Perdew–Burke–Ernzerhof generalized gradient approximation[54–56]. The projector augmented-wave potentials with the $2s^1$ electron for Li, $3d^8\ 4s^2$ electrons for Ni, $2s^2\ 2p^4$ electrons for O, $3d^7\ 4s^2$ electrons for Co and $2s^2\ 2p^1$ electrons for B were used. DFT + *U* was applied for the 3*d* orbitals of Ni (*U* = 6.0 eV and *J* = 0 eV) and Co (*U* = 3.4 eV and *J* = 0 eV) (refs. [57,58]). The plane-wave cutoff energy was set to be 520 eV and convergence was considered as reached when the residue atomic forces were less than 0.05 eV $Å^{-1}$. The (104) surface of the layered $LiNiO_2$ was simulated by a supercell that contained 20 Li, 20 Ni and 40 O atoms, with two surfaces separated by a 10 Å vacuum layer. The Brillouin zone was sampled using a Monkhorst–Pack scheme with a 3 × 3 × 3 **k**-point mesh. Amorphous Co_xB was simulated by a supercell that contained 70 Co and 32 B atoms (corresponding to a composition close to the experimentally measured $Co_{2.2}B$) and prepared by first-principles molecular dynamics at 2,500 K for 3.0 ps followed by quenching and relaxation at 0 K. The Brillouin zone was sampled using Monkhorst–Pack scheme with a 1 × 1 × 1 **k**-point mesh. To simulate the $Co_xB/LiNiO_2$ interface, an amorphous Co_xB slab that contained 35 Co and 16 B atoms were inserted between two (104) surfaces of a $LiNiO_2$ slab that contained 20 Li, 20 Ni and 40 O atoms. Their relative positions were adjusted so that the $Co_{35}B_{16}$ slab has a density is similar to that of the individually simulated amorphous Co_xB. The supercell was then heated to 2,500 K for 3.0 ps or 12.0 ps by first-principles molecular dynamics (here the positions 20 Li, 20 Ni and 40 O were fixed to avoid the melting of $LiNiO_2$), followed by quenching and relaxation at 0 K. In all the first-principles molecular dynamics calculations, the supercell size and shape were fixed and a time step of 1.5 fs was used. The Brillouin zone was sampled using Monkhorst–Pack scheme with a 1 × 1 × 1 **k**-point mesh for first-principles molecular dynamics and a 2 × 3 × 2 **k**-point mesh for 0 K relaxation. The atomic structures were visualized and plotted using VESTA[59]. The projected DOS of the O 2*p* orbitals were summed over p_x, p_y and p_z, including both spin-up and spin-down states.

Data availability

Data generated and analysed in this study are included in the manuscript and its Supplementary Information.

Received: 10 June 2020; Accepted: 18 January 2021;
Published online: 1 March 2021

References

1. Nitta, N., Wu, F., Lee, J. T. & Yushin, G. Li-ion battery materials: present and future. *Mater. Today* **18**, 252–264 (2015).
2. Kim, J. et al. Prospect and reality of Ni-rich cathode for commercialization. *Adv. Energy Mater.* **8**, 1702028 (2018).
3. Li, W., Erickson, E. M. & Manthiram, A. High-nickel layered oxide cathodes for lithium-based automotive batteries. *Nat. Energy* **5**, 26–34 (2020).
4. Edström, K., Gustafsson, T. & Thomas, J. O. The cathode–electrolyte interface in the Li-ion battery. *Electrochim. Acta* **50**, 397–403 (2004).
5. Sharifi-Asl, S., Lu, J., Amine, K. & Shahbazian-Yassar, R. Oxygen release degradation in Li-ion battery cathode materials: mechanisms and mitigating approaches. *Adv. Energy Mater.* **9**, 1900551 (2019).
6. Xie, Q., Li, W. & Manthiram, A. A Mg-doped high-nickel layered oxide cathode enabling safer, high-energy-density Li-ion batteries. *Chem. Mater.* **31**, 938–946 (2019).
7. Schipper, F. et al. From surface ZrO_2 coating to bulk Zr doping by high temperature annealing of nickel-rich lithiated oxides and their enhanced electrochemical performance in lithium ion batteries. *Adv. Energy Mater.* **8**, 1701682 (2018).
8. Xu, X. et al. Radially oriented single-crystal primary nanosheets enable ultrahigh rate and cycling properties of $LiNi_{0.8}Co_{0.1}Mn_{0.1}O_2$ cathode material for lithium-ion batteries. *Adv. Energy Mater.* **9**, 1803963 (2019).
9. Ofer, D., Pullen, A. W. & Sriramulu, S. Polycrystalline metal oxide, methods of manufacture thereof, and articles comprising the same. US patent 9,391,317 (2016).
10. Kim, J. et al. A highly stabilized nickel-rich cathode material by nanoscale epitaxy control for high-energy lithium-ion batteries. *Energy Environ. Sci.* **11**, 1449–1459 (2018).
11. Yan, P. et al. Tailoring grain boundary structures and chemistry of Ni-rich layered cathodes for enhanced cycle stability of lithium-ion batteries. *Nat. Energy* **3**, 600–605 (2018).
12. Xu, G.-L. et al. Building ultraconformal protective layers on both secondary and primary particles of layered lithium transition metal oxide cathodes. *Nat. Energy* **4**, 484–494 (2019).
13. Li, L. et al. Hidden subsurface reconstruction and its atomic origins in layered oxide cathodes. *Nano Lett.* **20**, 2756–2762 (2020).
14. Liu, H. et al. Intergranular cracking as a major cause of long-term capacity fading of layered cathodes. *Nano Lett.* **17**, 3452–3457 (2017).
15. Yan, P. et al. Coupling of electrochemically triggered thermal and mechanical effects to aggravate failure in a layered cathode. *Nat. Commun.* **9**, 2437 (2018).
16. Watanabe, S., Kinoshita, M., Hosokawa, T., Morigaki, K. & Nakura, K. Capacity fade of $LiAl_yNi_{1-x-y}Co_xO_2$ cathode for lithium-ion batteries during accelerated calendar and cycle life tests (surface analysis of $LiAl_yNi_{1-x-y}Co_xO_2$ cathode after cycle tests in restricted depth of discharge ranges). *J. Power Sources* **258**, 210–217 (2014).
17. Jung, R., Metzger, M., Maglia, F., Stinner, C. & Gasteiger, H. A. Chemical versus electrochemical electrolyte oxidation on NMC111, NMC622, NMC811, LNMO, and conductive carbon. *J. Phys. Chem. Lett.* **8**, 4820–4825 (2017).
18. Freiberg, A. T. S., Roos, M. K., Wandt, J., de Vivie-Riedle, R. & Gasteiger, H. A. Singlet oxygen reactivity with carbonate solvents used for Li-ion battery electrolytes. *J. Phys. Chem. A* **122**, 8828–8839 (2018).
19. Zhan, C., Wu, T., Lu, J. & Amine, K. Dissolution, migration, and deposition of transition metal ions in Li-ion batteries exemplified by Mn-based cathodes—a critical review. *Energy Environ. Sci.* **11**, 243–257 (2018).
20. Huang, Y. et al. Lithium manganese spinel cathodes for lithium-ion batteries. *Adv. Energy Mater.* **11**, 2000997 (2021).
21. Zhu, Z. et al. Gradient Li-rich oxide cathode particles immunized against oxygen release by a molten salt treatment. *Nat. Energy* **4**, 1049–1058 (2019).
22. Yan, P. et al. Injection of oxygen vacancies in the bulk lattice of layered cathodes. *Nat. Nanotechnol.* **14**, 602–608 (2019).
23. Armstrong, A. R. et al. Demonstrating oxygen loss and associated structural reorganization in the lithium battery cathode $Li[Ni_{0.2}Li_{0.2}Mn_{0.6}]O_2$. *J. Am. Chem. Soc.* **128**, 8694–8698 (2006).
24. House, R. A. et al. What triggers oxygen loss in oxygen redox cathode materials? *Chem. Mater.* **31**, 3293–3300 (2019).
25. Yoon, M. et al. Unveiling nickel chemistry in stabilizing high-voltage cobalt-rich cathodes for lithium-ion batteries. *Adv. Funct. Mater.* **30**, 1907903 (2020).
26. Jain, A. et al. Commentary: The Materials Project: a materials genome approach to accelerating materials innovation. *APL Mater.* **1**, 011002 (2013).
27. Mu, D. & Yang, C. Shen, B.-l. & Jiang, H. Oxidation resistance of borided pure cobalt. *J. Alloy. Compd* **479**, 629–633 (2009).
28. Yang, Y., Kushima, A., Han, W., Xin, H. & Li, J. Liquid-like, self-healing aluminum oxide during deformation at room temperature. *Nano Lett.* **18**, 2492–2497 (2018).
29. Li, J., Lenosky, T. J., Först, C. J. & Yip, S. Thermochemical and mechanical stabilities of the oxide scale of ZrB_2+SiC and oxygen transport mechanisms. *J. Am. Ceram. Soc.* **91**, 1475–1480 (2008).

30. Hasegawa, R. & Ray, R. Iron–boron metallic glasses. *J. Appl. Phys.* **49**, 4174–4179 (1978).
31. Gaskell, P. H. A new structural model for amorphous transition metal silicides, borides, phosphides and carbides. *J. Non-Cryst. Solids* **32**, 207–224 (1979).
32. Masa, J. et al. Amorphous cobalt boride (Co_2B) as a highly efficient nonprecious catalyst for electrochemical water splitting: oxygen and hydrogen evolution. *Adv. Energy Mater.* **6**, 1502313 (2016).
33. Deng, J. et al. Co–B nanoflakes as multifunctional bridges in $ZnCo_2O_4$ micro-/nanospheres for superior lithium storage with boosted kinetics and stability. *Adv. Energy Mater.* **9**, 1803612 (2019).
34. Jiang, B. et al. A mesoporous non-precious metal boride system: synthesis of mesoporous cobalt boride by strictly controlled chemical reduction. *Chem. Sci.* **11**, 791–796 (2020).
35. Chen, Z. et al. Study of cobalt boride-derived electrocatalysts for overall water splitting. *Int. J. Hydrog. Energy* **43**, 6076–6087 (2018).
36. Zhang, C. et al. Revealing the role of NH_4VO_3 treatment in Ni-rich cathode materials with improved electrochemical performance for rechargeable lithium-ion batteries. *Nanoscale* **10**, 8820–8831 (2018).
37. Yu, Y. et al. Optimal annealing of Al foil anode for prelithiation and full-cell cycling in Li-ion battery: the role of grain boundaries in lithiation/delithiation ductility. *Nano Energy* **67**, 104274 (2020).
38. Miller, D. J., Proff, C., Wen, J. G., Abraham, D. P. & Bareño, J. Observation of microstructural evolution in Li battery cathode oxide particles by in situ electron microscopy. *Adv. Energy Mater.* **3**, 1098–1103 (2013).
39. Kondrakov, A. O. et al. Anisotropic lattice strain and mechanical degradation of high- and low-nickel NCM cathode materials for Li-ion batteries. *J. Phys. Chem. C.* **121**, 3286–3294 (2017).
40. Kim, J. et al. Controllable solid electrolyte interphase in nickel-rich cathodes by an electrochemical rearrangement for stable lithium-ion batteries. *Adv. Mater.* **30**, 1704309 (2018).
41. Zhao, W. et al. High voltage operation of Ni-rich NMC cathodes enabled by stable electrode/electrolyte interphases. *Adv. Energy Mater.* **8**, 1800297 (2018).
42. Yoon, W.-S. et al. Investigation of the charge compensation mechanism on the electrochemically Li-ion deintercalated $Li_{1-x}Co_{1/3}Ni_{1/3}Mn_{1/3}O_2$ electrode system by combination of soft and hard X-ray absorption spectroscopy. *J. Am. Chem. Soc.* **127**, 17479–17487 (2005).
43. Lin, F. et al. Profiling the nanoscale gradient in stoichiometric layered cathode particles for lithium-ion batteries. *Energy Environ. Sci.* **7**, 3077–3085 (2014).
44. Yang, L., Ravdel, B. & Lucht, B. L. Electrolyte reactions with the surface of high voltage $LiNi_{0.5}Mn_{1.5}O_4$ cathodes for lithium-ion batteries. *Electrochem. Solid-State Lett.* **13**, A95–A97 (2010).
45. Zheng, J. et al. Highly stable operation of lithium metal batteries enabled by the formation of a transient high-concentration electrolyte layer. *Adv. Energy Mater.* **6**, 1502151 (2016).
46. Li, W. et al. Dynamic behaviour of interphases and its implication on high-energy-density cathode materials in lithium-ion batteries. *Nat. Commun.* **8**, 14589 (2017).
47. Nguyen, T. T. D. et al. Understanding the thermal runaway of Ni-rich lithium-ion batteries. *World Electr. Veh. J.* **10**, 79 (2019).
48. Lin, D., Liu, Y. & Cui, Y. Reviving the lithium metal anode for high-energy batteries. *Nat. Nanotechnol.* **12**, 194–206 (2017).
49. Seo, D.-H. et al. The structural and chemical origin of the oxygen redox activity in layered and cation-disordered Li-excess cathode materials. *Nat. Chem.* **8**, 692–697 (2016).
50. Luo, K. et al. Charge-compensation in 3*d*-transition-metal-oxide intercalation cathodes through the generation of localized electron holes on oxygen. *Nat. Chem.* **8**, 684–691 (2016).
51. Hashigami, S. et al. Improvement of cycleability and rate-capability of $LiNi_{0.5}Co_{0.2}Mn_{0.3}O_2$ cathode materials coated with lithium boron oxide by an antisolvent precipitation method. *Chem. Sel.* **4**, 8676–8681 (2019).
52. Park, J.-H. et al. Effect of residual lithium rearrangement on Ni-rich layered oxide cathodes for lithium-ion batteries. *Energy Technol.* **6**, 1361–1369 (2018).
53. Kang, S. J., Mori, T., Narizuka, S., Wilcke, W. & Kim, H.-C. Deactivation of carbon electrode for elimination of carbon dioxide evolution from rechargeable lithium–oxygen cells. *Nat. Commun.* **5**, 3937 (2014).
54. Kresse, G. & Joubert, D. From ultrasoft pseudopotentials to the projector augmented-wave method. *Phys. Rev. B: Condens. Matter Mater. Phys.* **59**, 1758 (1999).
55. Kresse, G. & Furthmüller, J. Efficiency of ab-initio total energy calculations for metals and semiconductors using a plane-wave basis set. *Comput. Mater. Sci.* **6**, 15–50 (1996).
56. Perdew, J. P., Burke, K. & Ernzerhof, M. Generalized gradient approximation made simple. *Phys. Rev. Lett.* **77**, 3865–3868 (1996).
57. Dudarev, S. L., Botton, G. A., Savrasov, S. Y., Humphreys, C. J. & Sutton, A. P. Electron-energy-loss spectra and the structural stability of nickel oxide: an LSDA + *U* study. *Phys. Rev. B* **57**, 1505–1509 (1998).
58. Jain, A. et al. Formation enthalpies by mixing GGA and GGA + *U* calculations. *Phys. Rev. B* **84**, 045115 (2011).
59. Momma, K. & Izumi, F. VESTA 3 for three-dimensional visualization of crystal, volumetric and morphology data. *J. Appl. Crystallogr.* **44**, 1272–1276 (2011).

Acknowledgements

This work was supported by the Korea Institute of Energy Technology Evaluation and Planning (KETEP) and the Ministry of Trade, Industry & Energy (MOTIE) of the Republic of Korea (no. 20172410100140). 2020 Research Funds (1.200029.1) of the Ulsan National Institute of Science and Technology (UNIST) is also acknowledged. Y.D. and J.L. acknowledge support from the Department of Energy, Basic Energy Sciences, under award no. DE-SC0002633 (Chemomechanics of Far-From-Equilibrium Interfaces).

Author contributions

M.Y., Y.D., J.L. and J.C. conceived the project. M.Y. synthesized the materials and conducted the electrochemical testing. Y.D. conducted the simulations and theoretical analysis. M.Y. and J.H. conducted ex situ and in situ XRD measurements and analysis. H.C. and J.S. conducted the focused ion beam, TEM, SEM and XPS measurements. S.J.K. provided equipment for the DEMS measurements. M.Y. and K.A. assembled and tested the pouch-type full-cells. M.Y. and Y.D. analysed the data. M.Y., Y.D., J.L. and J.C. wrote the paper. All the authors discussed and contributed to the writing.

Competing interests

The authors declare no competing interests.

Additional information

Supplementary information The online version contains supplementary material available at https://doi.org/10.1038/s41560-021-00782-0.

Correspondence and requests for materials should be addressed to J.L. or J.C.

Peer review information *Nature Energy* thanks Payam Kaghazchi, David Wood III and the other, anonymous, reviewer(s) for their contribution to the peer review of this work.

Reprints and permissions information is available at www.nature.com/reprints.

Publisher's note Springer Nature remains neutral with regard to jurisdictional claims in published maps and institutional affiliations.

nature portfolio

https://doi.org/10.1038/s41560-021-00782-0

Supplementary information

Reactive boride infusion stabilizes Ni-rich cathodes for lithium-ion batteries

In the format provided by the authors and unedited

Supplementary information

Reactive boride infusion stabilizes Ni-rich cathodes for lithium-ion batteries

Moonsu Yoon[1,†], Yanhao Dong[2,†], Jaeseong Hwang[1], Jaekyung Sung[1], Hyungyeon Cha[1], Kihong Ahn[1], Yimeng Huang[3], Seok Ju Kang[1], Ju Li[2,3,*], Jaephil Cho[1,*]

[1]*School of Energy and Chemical Engineering, Ulsan National Institute of Science and Technology (UNIST), 50 UNIST-gil, Ulsan 44919, Republic of Korea*

[2]*Department of Nuclear Science and Engineering, Massachusetts Institute of Technology, Cambridge, Massachusetts 02139, United States*

[3]*Department of Materials Science and Engineering, Massachusetts Institute of Technology, Cambridge, Massachusetts 02139, United States*

Table of contents

Supplementary Figures 1-33 Page 2-34

Supplementary Tables 1-9 Page 35-43

Supplementary References Page 44

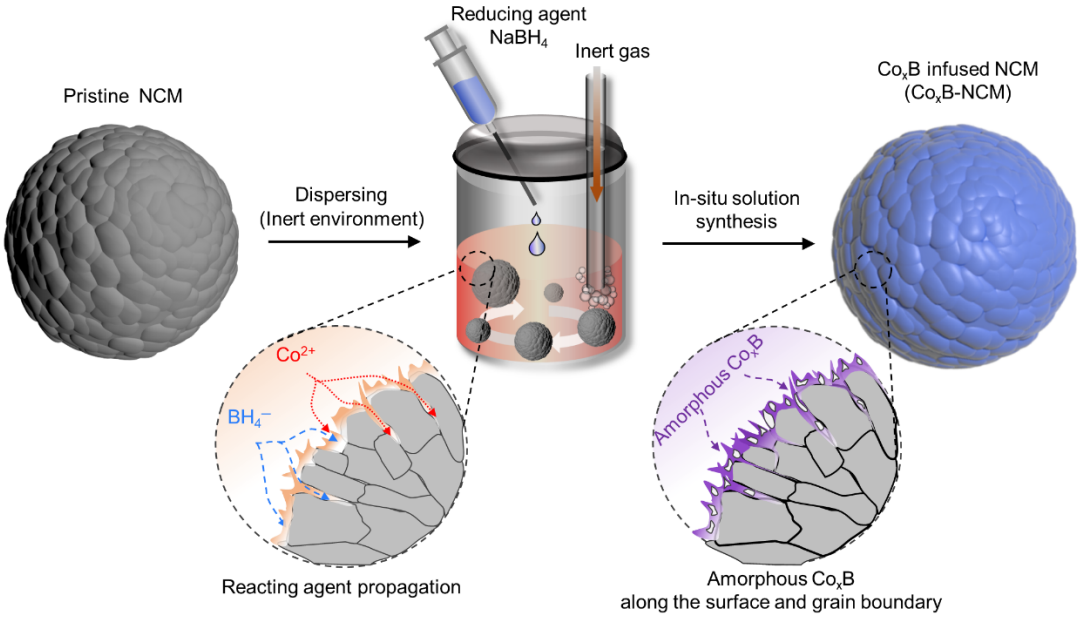

Supplementary Figure 1 | Schematic synthesis route of Co_xB coating/infusion on NCM cathode material.

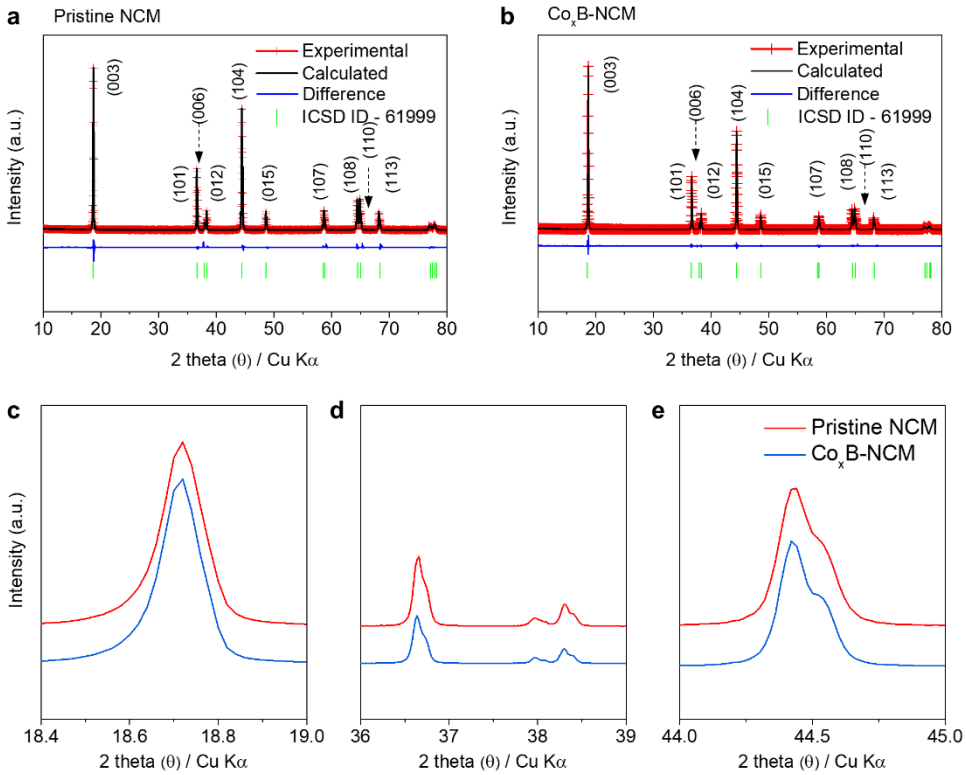

Supplementary Figure 2 | Rietveld refinement of XRD patterns for (a) pristine NCM and (b) Co_xB-NCM. Fitting details available in Supplementary Table 2. (c-e) Magnified XRD patterns at selected angles.

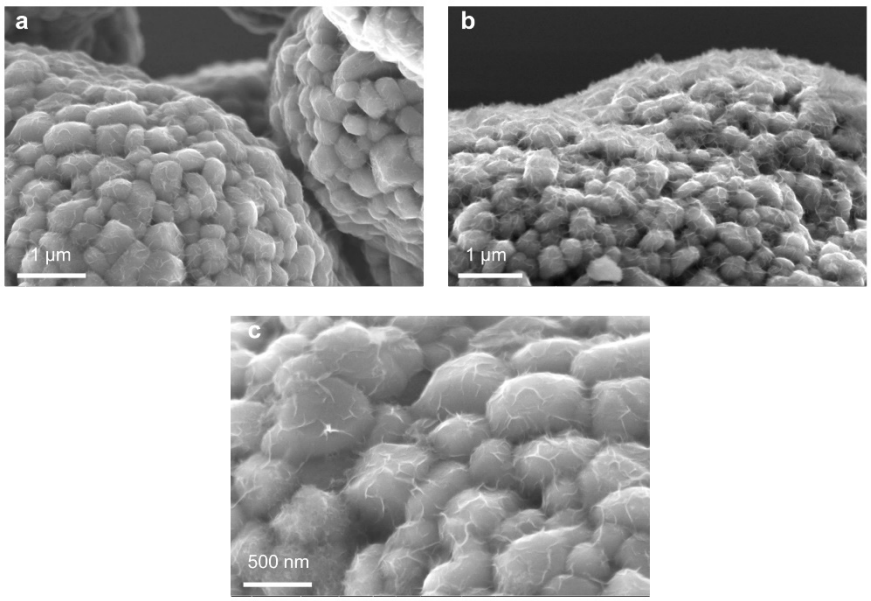

Supplementary Figure 3 | (a-c) SEM images showing NCM particles uniformly covered by fuzzy Co_xB coating layer.

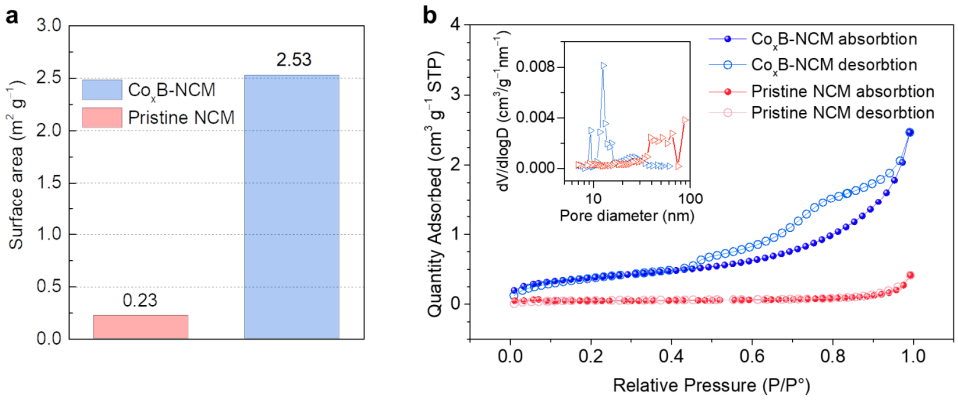

Supplementary Figure 4 | (a) Specific surface area of each pristine NCM and Co_xB-NCM cathode particle. (b) BET curve of each pristine NCM and Co_xB-NCM cathode particle. Inset: pore-size distribution.

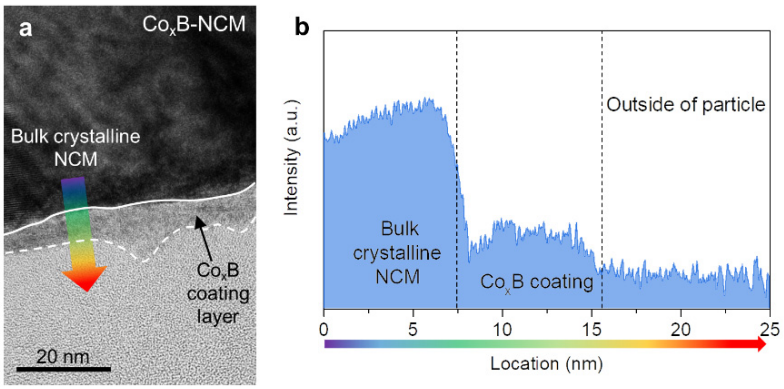

Supplementary Figure 5 | (a) TEM image of Co_xB-NCM covered by Co_xB coating layer and (b) the corresponding contrast intensity profile along the scan direction in (a).

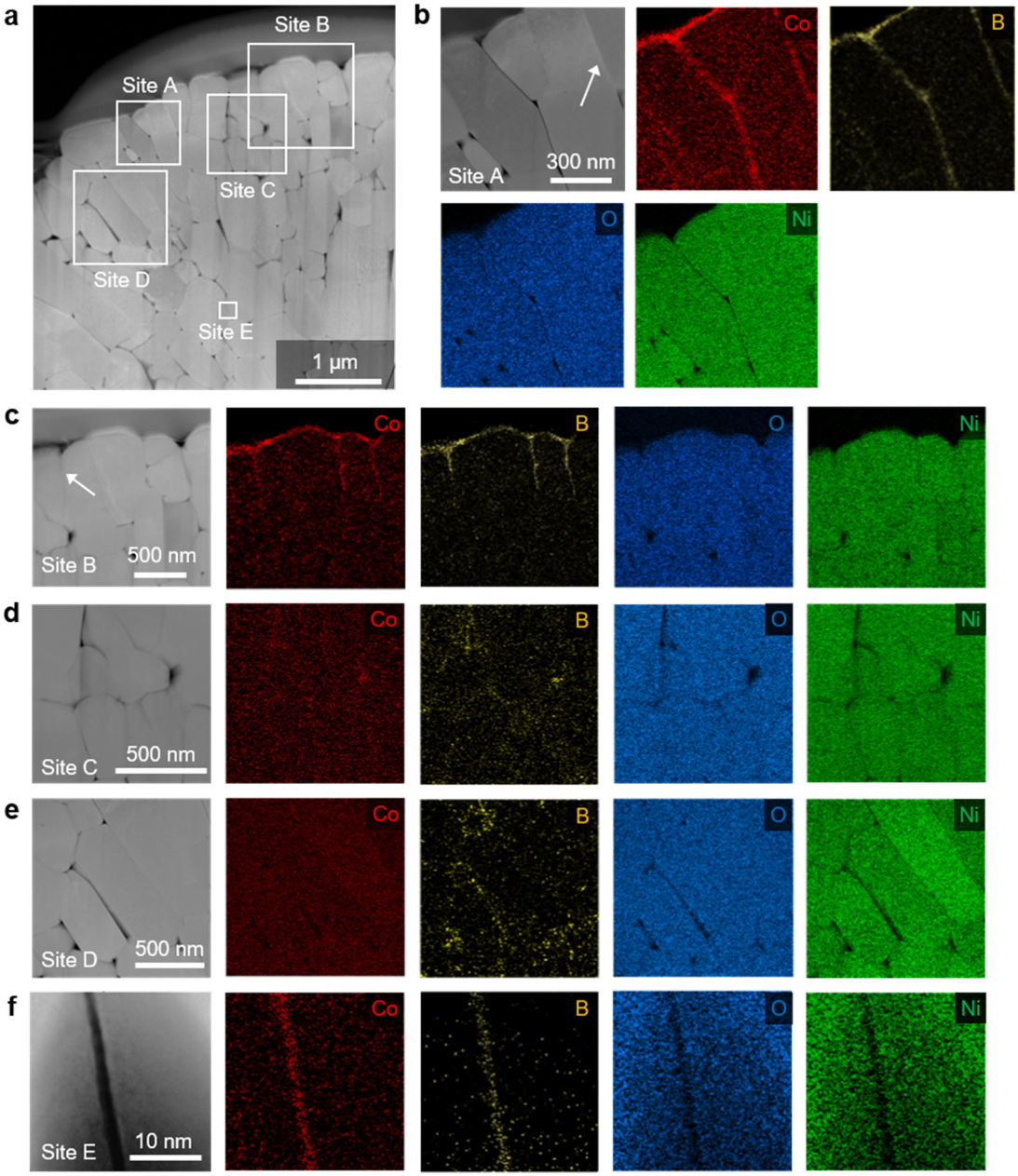

Supplementary Figure 6 | First set of TEM results confirming Co_xB coverage/infusion on surface/grain boundaries of NCM particles. (a) HAADF-STEM image of the cross-sectioned Co_xB-NCM secondary particle, and (b-f) the corresponding EDS element mapping of Co, B, O, Ni on the selected sites A-E in (a).

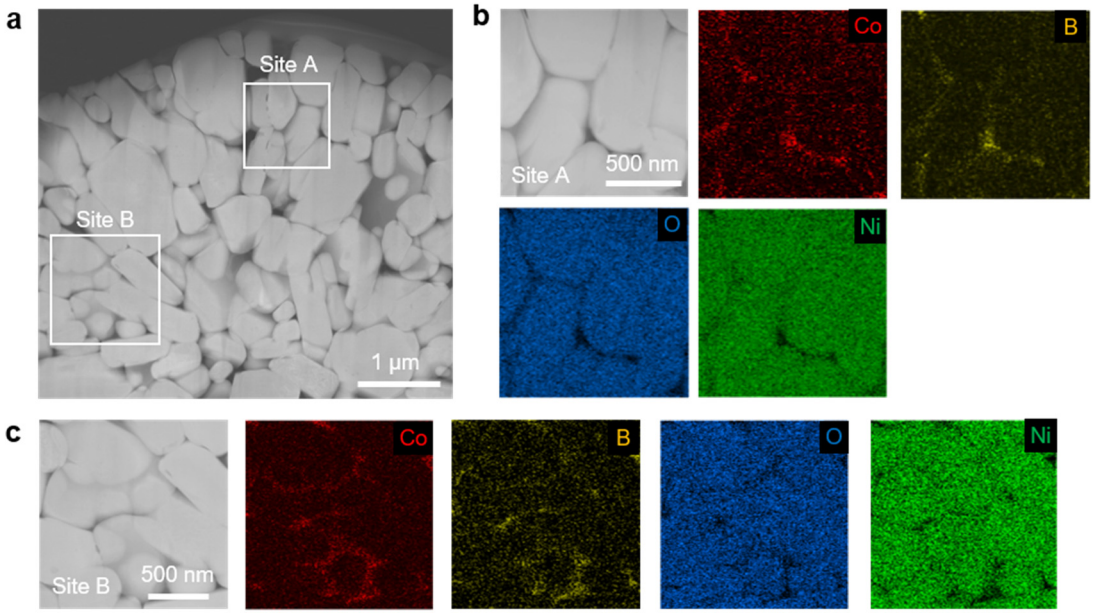

Supplementary Figure 7 | Second set of TEM results confirming Co_xB infusion into inner grain boundaries of NCM particles. (a) HAADF-STEM image of the cross-sectioned Co_xB-NCM secondary particle, and (b and c) the corresponding EDS element mapping of Co, B, O, Ni on the selected sites A and B in (a).

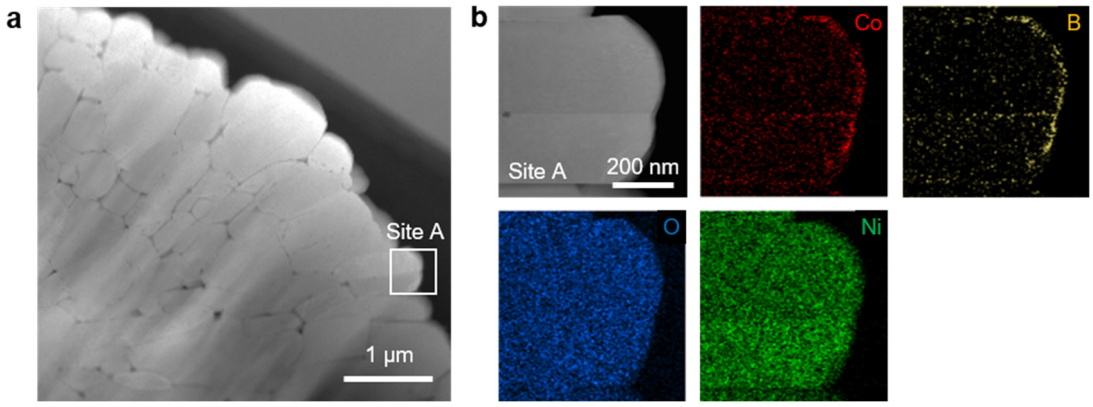

Supplementary Figure 8 | Third set of TEM results confirming Co_xB coverage/infusion on surface/grain boundaries of NCM particles. (a) HAADF-STEM image of the cross-sectioned Co_xB-NCM secondary particle, and (b) the corresponding EDS element mapping of Co, B, O, Ni on the selected site A in (a).

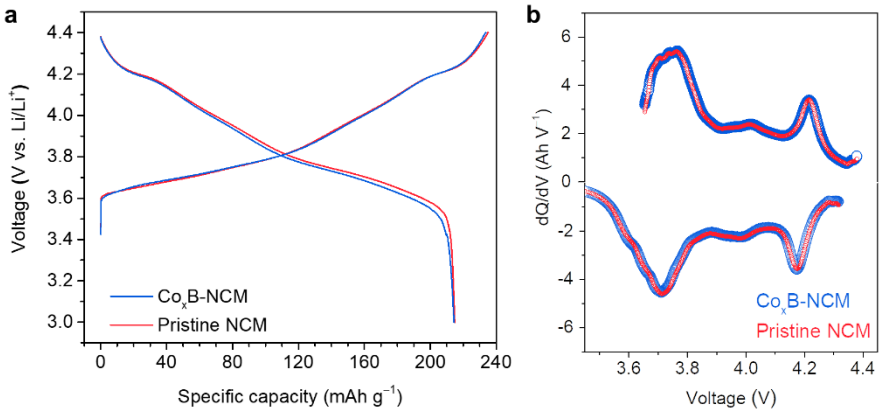

3.0~4.4V	Charge capacity (mAh g^{-1})	Discharge capacity (mAh g^{-1})	Coulombic efficiency (%)
Co_xB-NCM	234	214	91.5
Pristine NCM	235	215	91.5

Supplementary Figure 9 | First-cycle charge-discharge profile (i.e., formation cycle) and corresponding differential capacity versus voltage (*dQ/dV*) plot of Co_xB-NCM and pristine NCM at 0.1 C between 3.0 V and 4.4 V (vs. Li/Li^+) at 25°C.

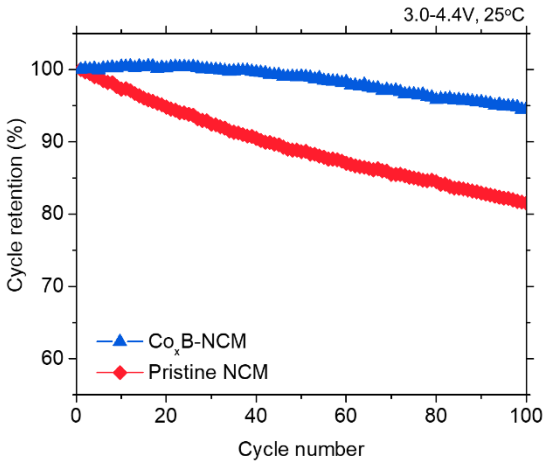

	1st cycle discharge capacity (mAh g^{-1})	100th cycle discharge capacity (mAh g^{-1})	Retention (%)
Co$_x$B-NCM	200	188	94.2
Pristine NCM	201	163	81.5

Supplementary Figure 10 | Cycling performance of Co$_x$B-NCM and pristine NCM at 0.5 C between 3.0 V and 4.4 V (vs. Li/Li$^+$) at 25°C.

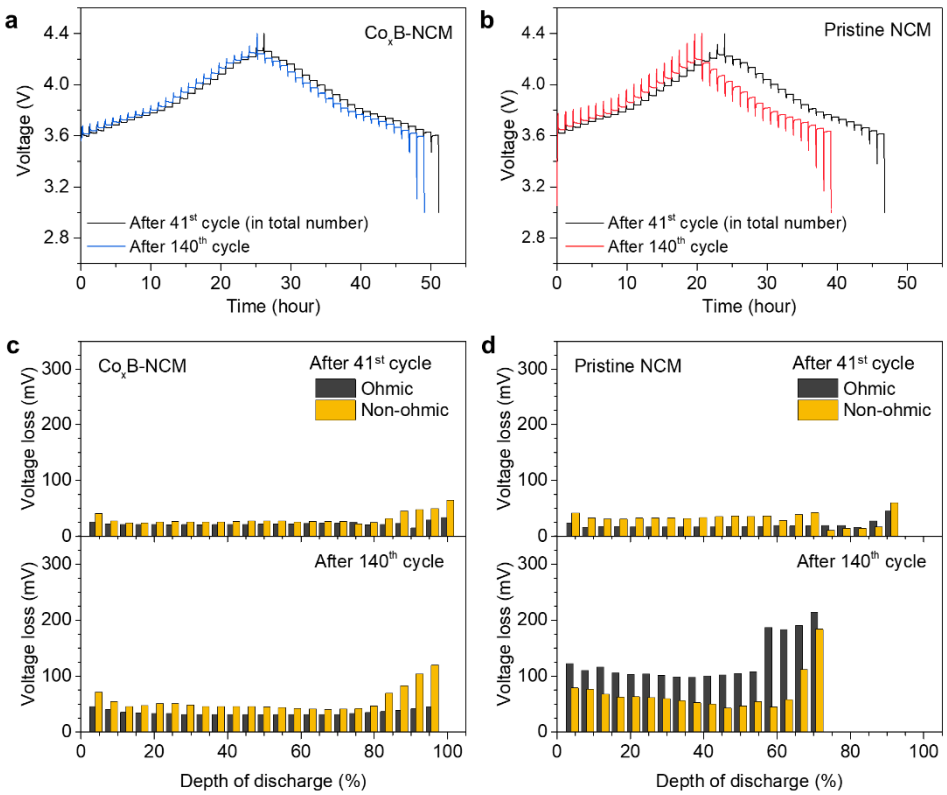

Supplementary Figure 11 | Galvanostatic intermittent titration technique (GITT) measurements on Co$_x$B-NCM and pristine NCM after certain cycles during 1 C cycling in **Fig. 3a**. The voltage profiles after first (41st cycle in total number of cycling) and last cycle (140th cycle in total number of cycling) for (a) Co$_x$B-NCM and (b) pristine NCM. The ohmic and non-ohmic voltage losses were separately plotted as a function of depth of discharge in (c) for Co$_x$B-NCM and (d) for pristine NCM.

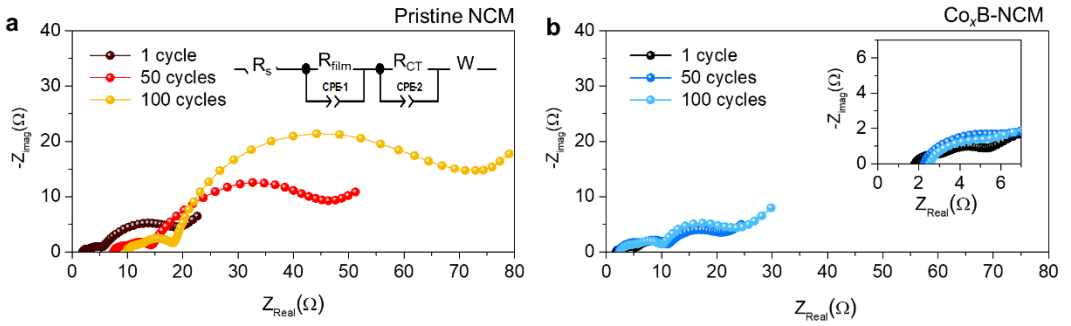

	1 cycle	
Sample	Pristine NCM	Co_xB-NCM
R_s (Ω)	2.67	1.85
R_{film} (Ω)	8.56	3.57
R_{CT} (Ω)	20.35	6.33

	50 cycles	
Sample	Pristine NCM	Co_xB-NCM
R_s (Ω)	8.48	2.55
R_{film} (Ω)	10.66	5.87
R_{CT} (Ω)	40.87	14.83

	100 cycles	
Sample	Pristine NCM	Co_xB-NCM
R_s (Ω)	10.38	2.58
R_{film} (Ω)	14.22	6.12
R_{CT} (Ω)	54.87	16.34

Supplementary Figure 12 | Electrochemical impedance spectroscopy (EIS) measurements on (a) pristine NCM and (b) Co_xB-NCM after 1 (41^{st} cycle in total number of cycling), 50 (90^{th} cycle in total number of cycling) and 100 cycles (140^{th} cycle in total number of cycling) during 1 C cycling in **Fig. 3a**. Insets: equivalent circuits. Fitted results are listed. Note R_{ct} contributes most to the impedance of cycled cathodes.

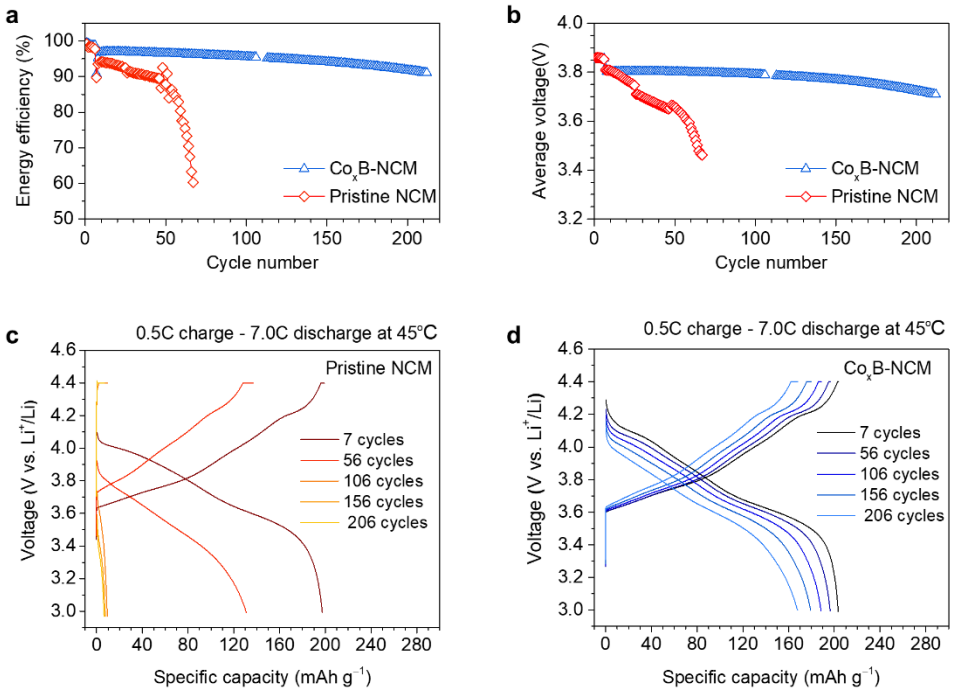

Supplementary Figure 13 | (a) Energy efficiency, (b) average discharge voltage, and voltage profiles of (c) pristine NCM and (d) Co_xB-NCM during 7 C-discharge cycling tests in **Fig. 3d** between 3.0 V and 4.4 V (vs. Li/Li^+) at 45°C. Charge rate is set as 0.5 C.

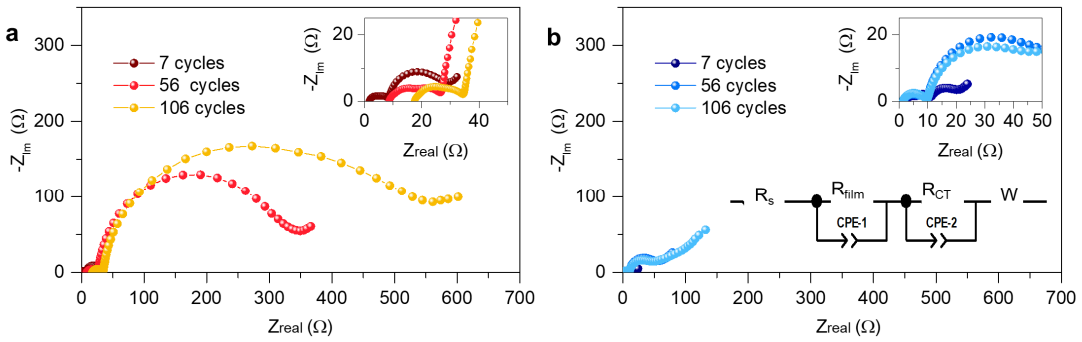

	7 cycles	
Sample	Pristine NCM	Co_xB-NCM
R_s (Ω)	2.09	1.36
R_{film} (Ω)	10.11	4.88
R_{CT} (Ω)	21.22	12.87

	56 cycles	
Sample	Pristine NCM	Co_xB-NCM
R_s (Ω)	12.77	1.5
R_{film} (Ω)	18.76	9.84
R_{CT} (Ω)	280.5	45.87

	106 cycles	
Sample	Pristine NCM	Co_xB-NCM
R_s (Ω)	18.9	2.12
R_{film} (Ω)	22.44	12.55
R_{CT} (Ω)	552.4	59.5

Supplementary Figure 14 | Electrochemical impedance spectroscopy (EIS) measurements on (a) pristine NCM and (b) Co_xB-NCM after 7, 56 and 106 cycles of 7 C-discharge cycling between 3.0 V and 4.4 V (vs. Li/Li^+) at 45 °C. (Charge rate is set as 0.5 C.) Insets: Magnified EIS data and equivalent circuit. Fitted results are listed. Note R_{ct} contributes most to the impedance of cycled cathodes.

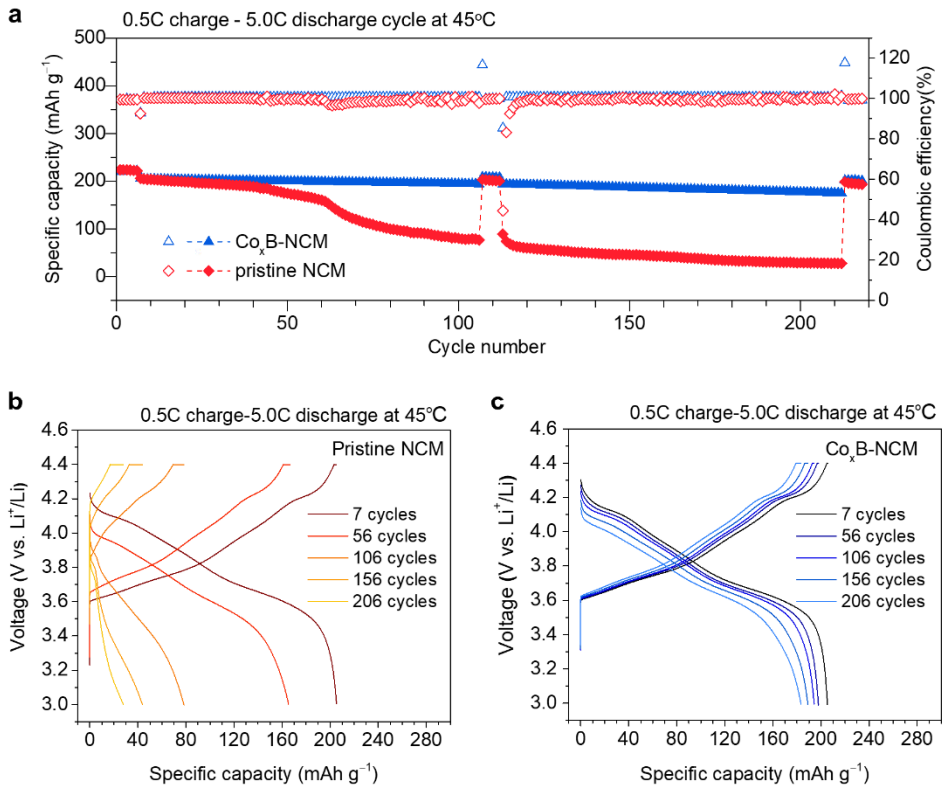

Supplementary Figure 15 | (a) Cycling performance and coulombic efficiency of pristine NCM and Co$_x$B-NCM at 5 C discharge rate between 3.0 V and 4.4 V (vs. Li/Li$^+$) at 45°C. (Charge rate is set as 0.5 C.) Also shown are discharge-discharge curves of (b) pristine NCM and (c) Co$_x$B-NCM after certain cycles.

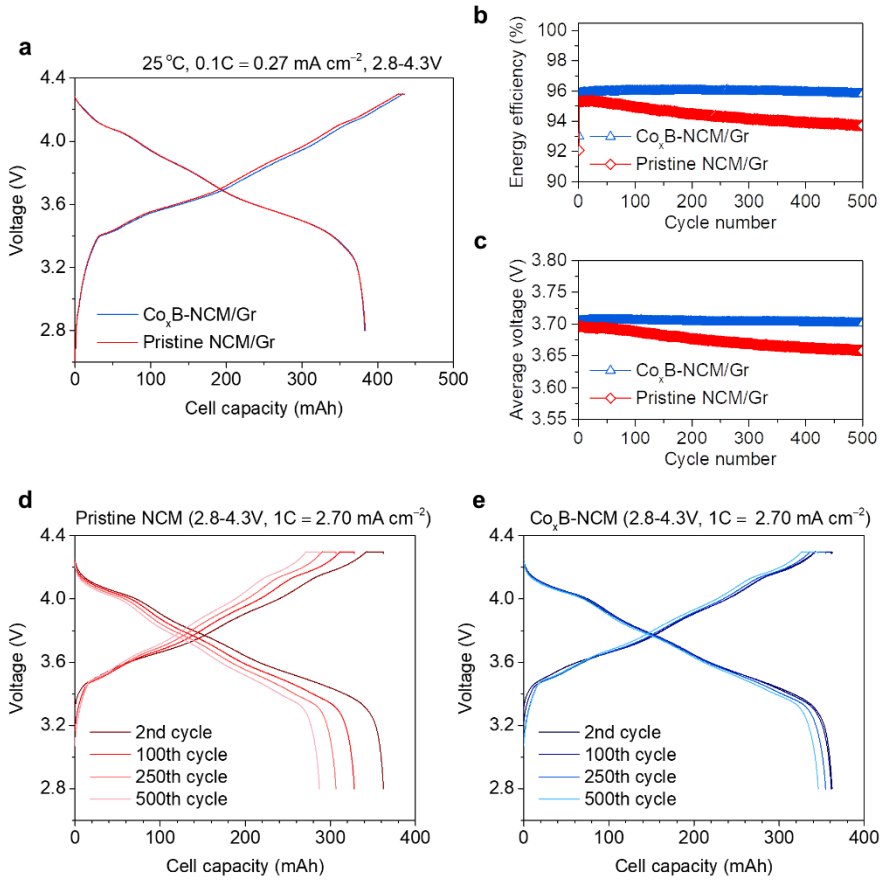

Supplementary Figure 16 | Electrochemical performance of Co_xB-NCM/Gr and pristine NCM/Gr full cells tested in the voltage range of 2.8−4.3V at 25°C. (a) Initial full-cell formation step performed at 2.8–4.3 V with a charge and discharge C-rate of 0.1 C. (b) Energy efficiency, (c) average discharge voltage, and voltage profiles of (d) pristine NCM/Gr and (e) Co_xB-NCM/Gr full cells during 500 cycles (Galvanostatic charge-discharge cycling was performed with a charge and discharge C-rate of 1.0 C ≈ 2.70 mA cm^{-2}).

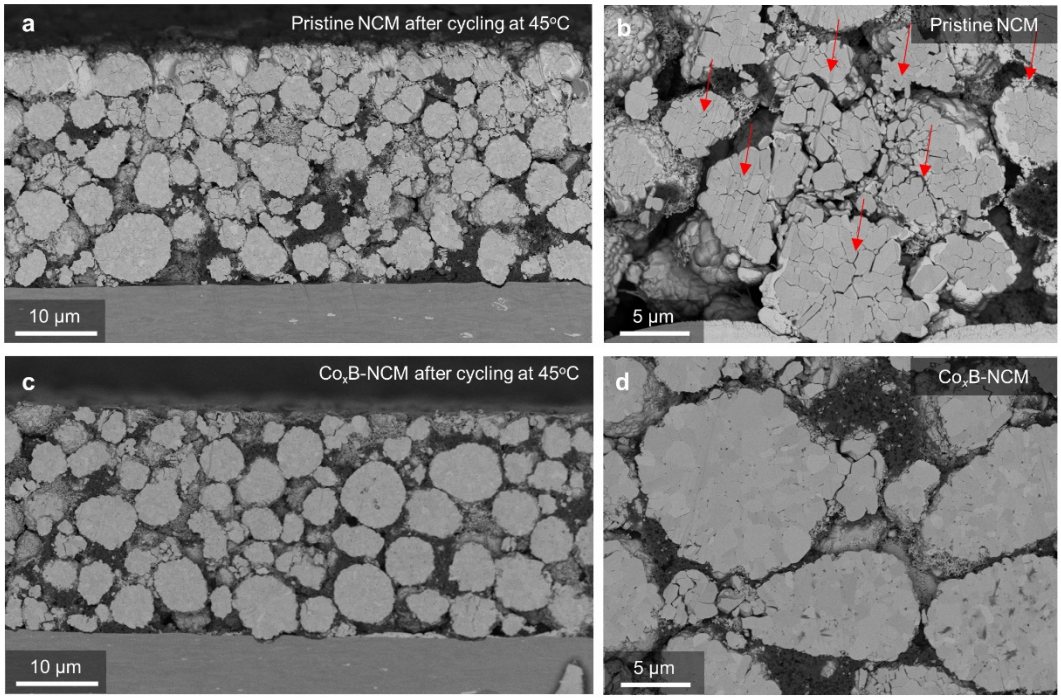

Supplementary Figure 17 | SEM images of cross-sectioned electrodes of (a,b) pristine NCM and (c,d) Co_xB-NCM after 200 cycles of 7 C-discharge cycling at 45°C.

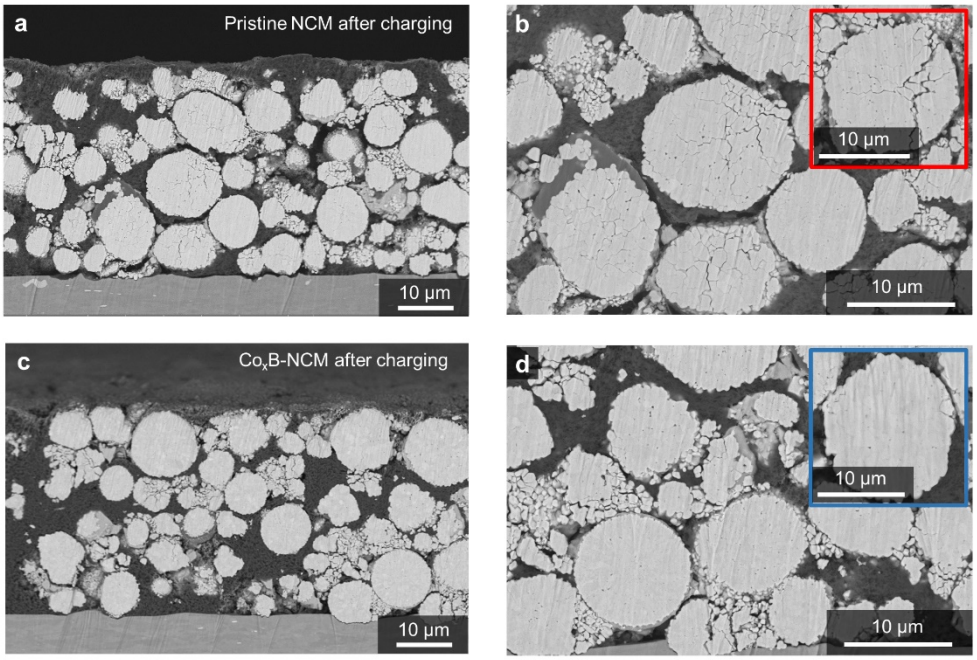

Supplementary Figure 18 | SEM images of cross-sectioned (a, b) pristine NCM and (c, d) Co_xB-NCM cathodes after the first charge to 4.4 V vs. Li^+/Li. Insets of (b, d) show low-magnification images.

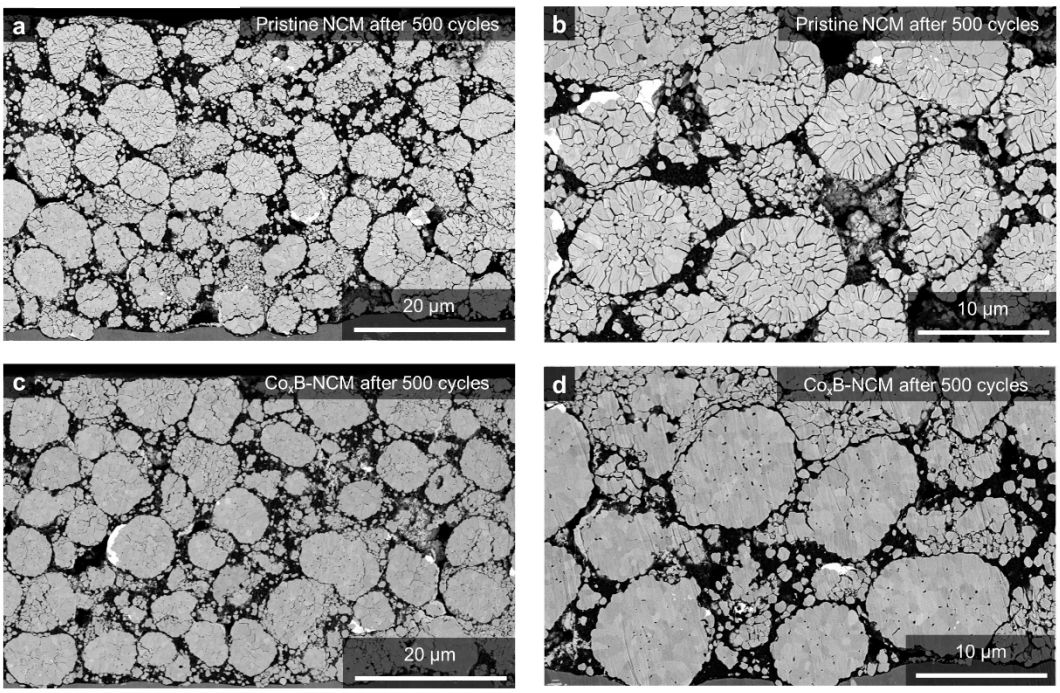

Supplementary Figure 19 | SEM images of cross-sectioned (a, b) pristine NCM and (c, d) Co_xB-NCM cathodes after 500 cycles in pouch-type full cells at 1.0 C/1.0 C in the voltage range of 2.8−4.3 V at 25°C.

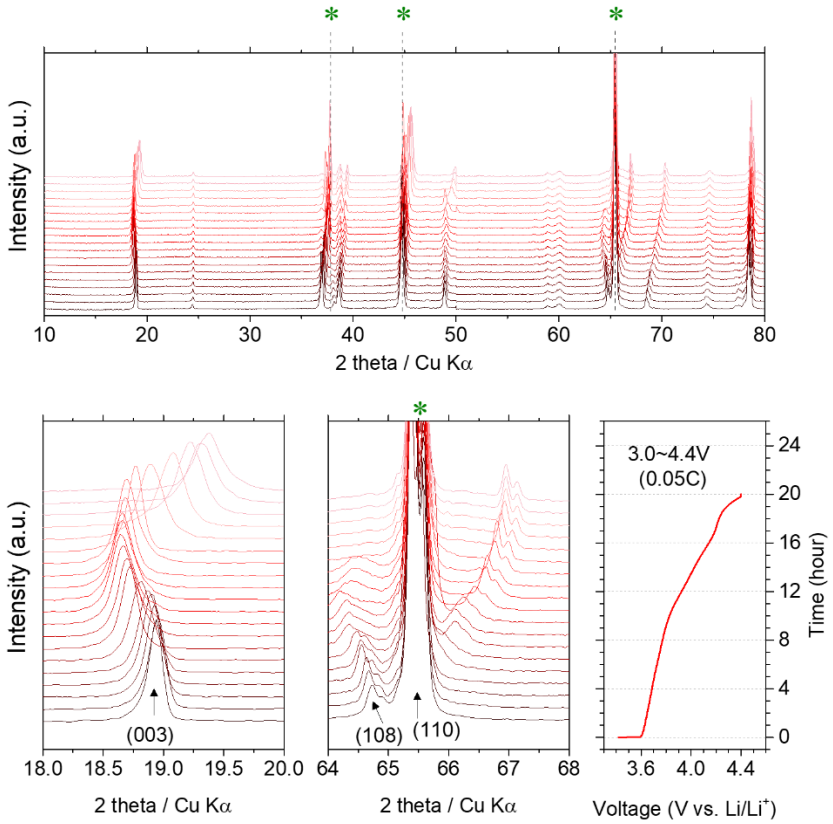

Supplementary Figure 20 | *In-situ* XRD patterns of pristine NCM during 0.05 C charge between 3.0 V and 4.4 V (vs. Li/Li^+) after the formation cycling at ambient conditions. The green asterisks represent the aluminum current collector.

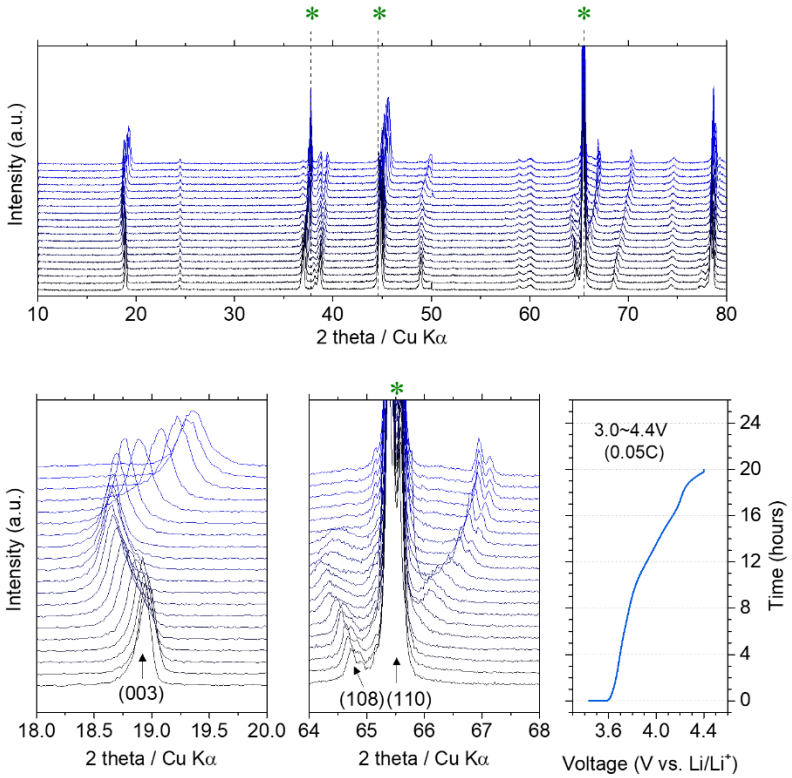

Supplementary Figure 21 | *In-situ* XRD patterns of Co_xB-NCM during 0.05 C charge between 3.0 V and 4.4 V (vs. Li/Li^+) after the formation cycling at ambient conditions. The green asterisks represent the aluminum current collector.

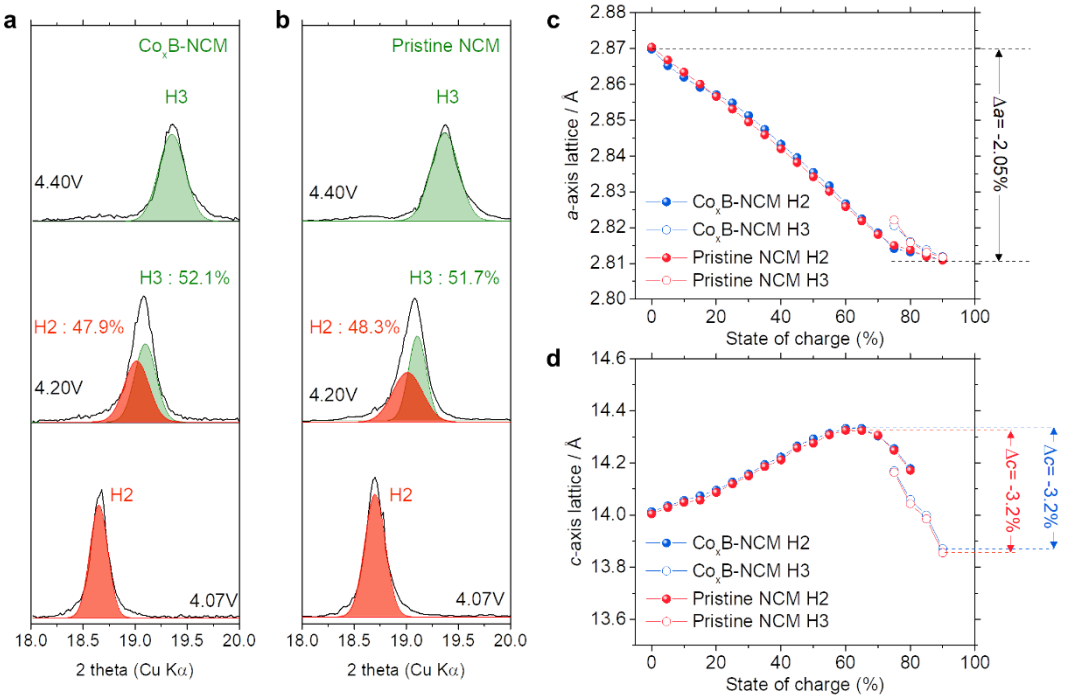

Supplementary Figure 22 | (003) reflections and calculated H2 and H3 percentage of (a) Co_xB-NCM and (b) pristine NCM at different charge voltages (vs. Li/Li^+) from *in situ* XRD data. Change in (c) *a*-axis and (d) *c*-axis lattice parameters of Co_xB-NCM and pristine NCM during as a function of the state of charge (SOC).

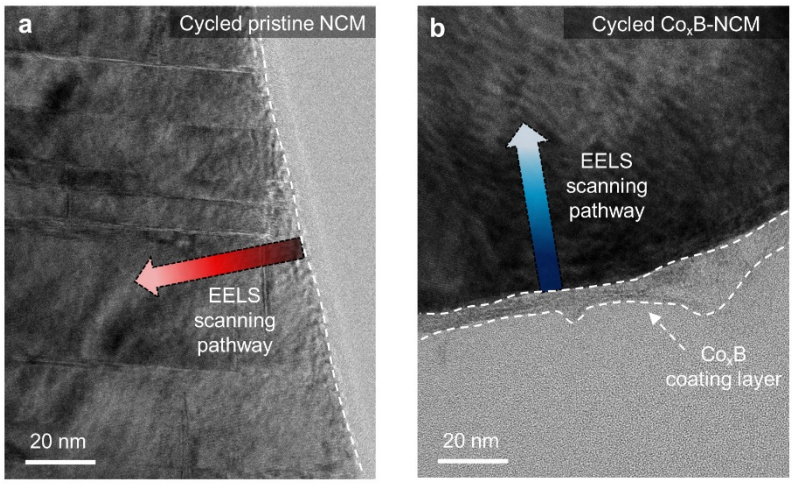

Supplementary Figure 23 | Schematic STEM-EELS scanning pathway (0 to 45 nm from outer surface) of (a) pristine NCM and (b) Co_xB-NCM after 200 cycles of 7 C-discharge cycling at 45°C, corresponding to EELS data in **Fig. 3c** and **3f**, respectively.

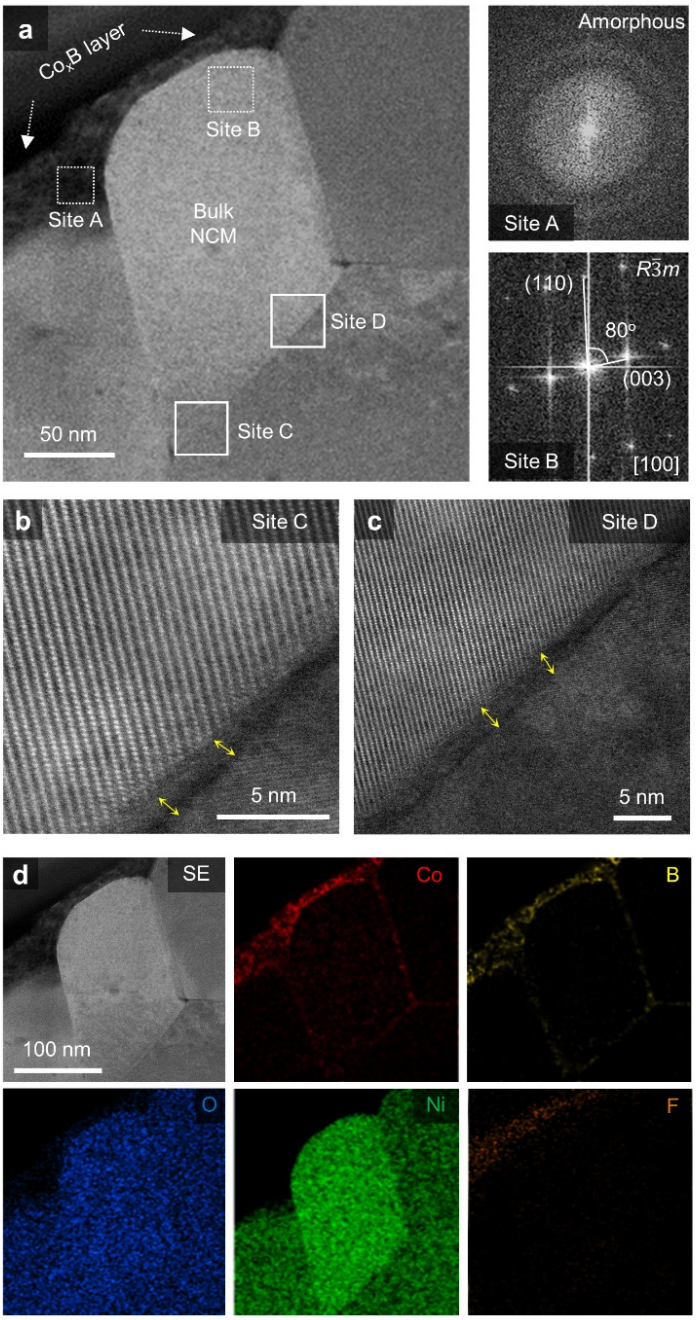

Supplementary Figure 24 | TEM results confirming the existence of Co_xB on the surface and at the grain boundaries of NCM particles after 500 cycles in pouch-type full cells at 1.0 C in the voltage range of 2.8−4.3 V at 25°C. (a) HAADF-STEM image of the cross-sectioned Co_xB-NCM secondary particle and corresponding FFT pattern for Co_xB layer (site A) and bulk NCM (site B). (b, c) High-magnification HAADF-STEM images of site C and D in (a), and (d) the corresponding EDS element mapping of Co, B, O, Ni and F on the selected sites in (a). The grain boundaries between two primary NCM particles are indicated by yellow arrows in (b and c).

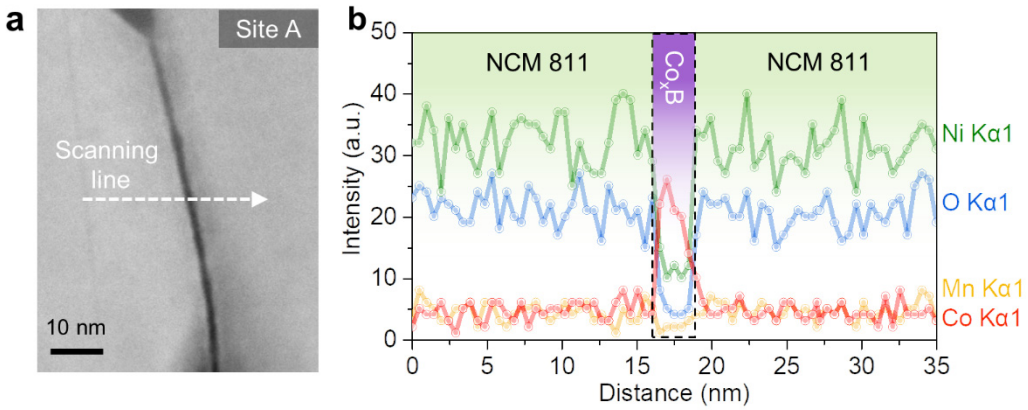

Supplementary Figure 25 | (a) HR-TEM and (b) EDS line-scan across the grain boundary showing Co_xB phase after 200 cycles of 7 C-discharge cycling at 45°C.

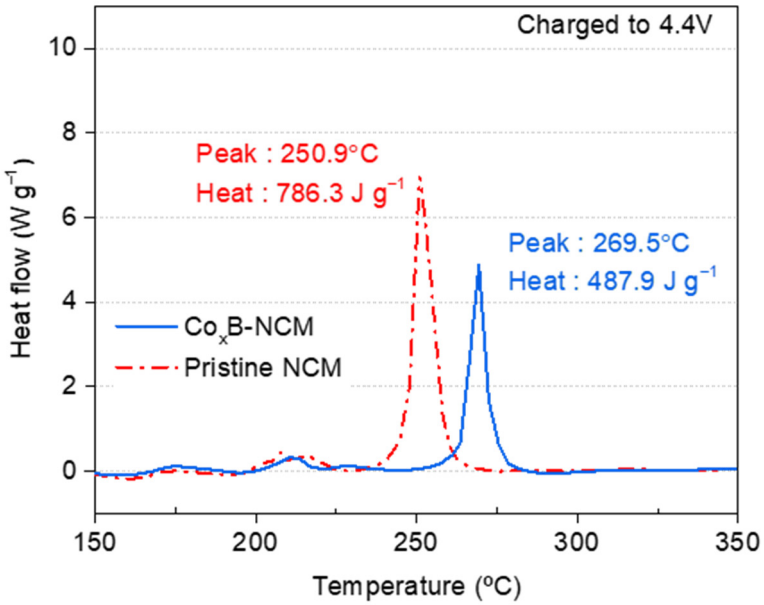

Supplementary Figure 26 | DSC measurement of Co_xB-NCM and pristine NCM charged to 4.4 V vs. Li/Li^+.

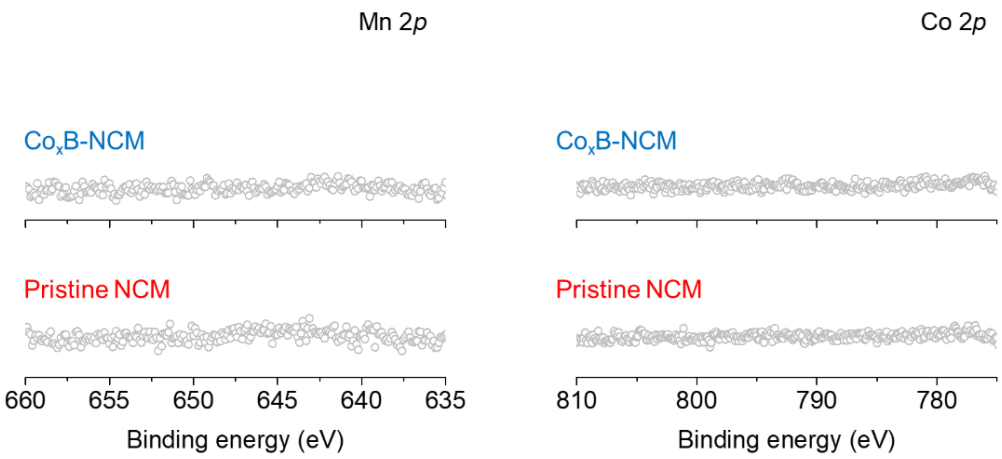

Supplementary Figure 27 | XPS spectra for Mn 2*p* and Co 2*p* of the LMAs paired with Co_xB-NCM and pristine NCM after 200 cycles of 7 C-discharge cycling at 45°C.

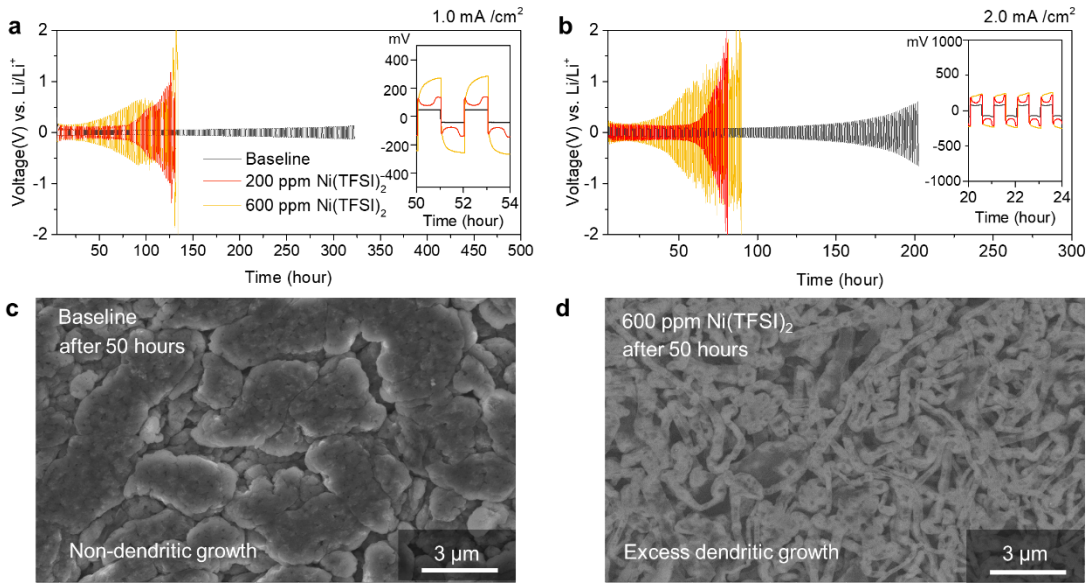

Supplementary Figure 28 | Electrochemical performance for symmetrical Li/Li symmetric cells using the electrolytes containing 0, 200 and 600 ppm $Ni(TFSI)_2$. Galvanostatic cycling test performed at a Li plating/stripping current density of (a) 1.0 and (b) 2.0 mA cm^{-2} with a cycling capacity of 2.0 mAh cm^{-2} (corresponding to 2 h or 1 h for each step, respectively). Top-view SEM images of cycled LMA using electrolyte containing (c) 0 and (d) 600ppm $Ni(TFSI)_2$ after 50 hours cycled at 1.0 mA cm^{-2}. Insets of (c, d): photographs of cycled lithium metal anodes from disassembled Li/Li symmetric cells.

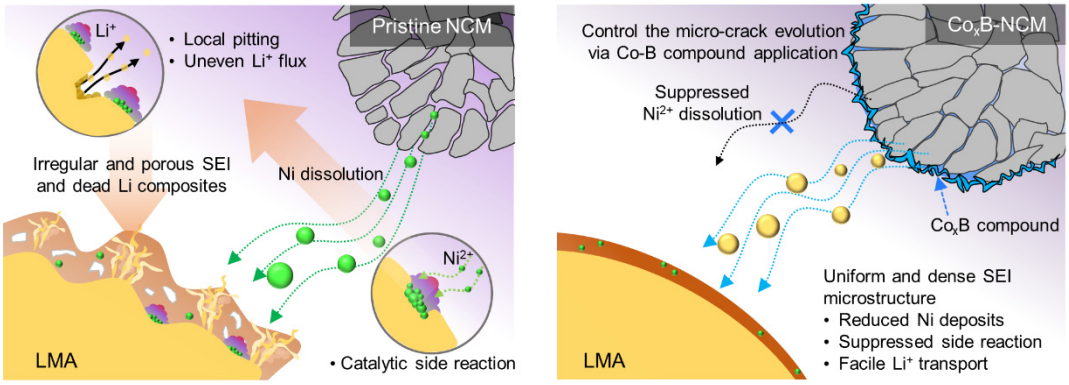

Supplementary Figure 29 | Schematic cross-over effect on LMA. Pristine NCM suffers from severe side reactions and intergranular cracking, generation of extensive fresh surfaces and more transition metal dissolution, which migrates and precipitates at LMA. The precipitated transition metals (e.g., Ni) affects stability of SEI. During electrochemical cycling, continuous breakdown and reformation of unstable SEI layer creates porous "dead" Li layer with irregular morphology and degrades the electrochemical performance of LMA. In contrast, side reactions and intergranular cracking are mitigated in Co_xB-NCM, which results in less transition metal dissolution and stable dense LMA.

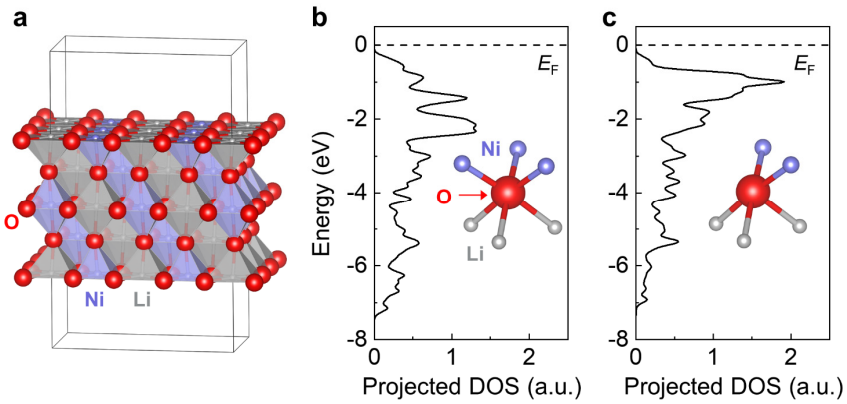

Supplementary Figure 30 | (a) atomic structure simulated $LiNiO_2$ (104) surface. Projected density of states and schematic local environment (insets of b-c) of (b) lattice oxygen coordinated by 3 Ni and 3 Li, and (c) surface oxygen coordinated by 2 Ni and 3 Li.

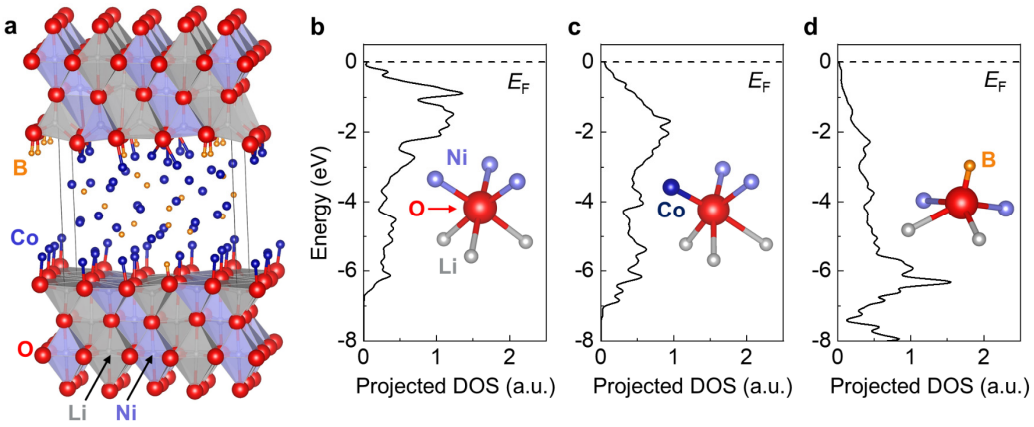

Supplementary Figure 31 | (a) Atomic structure interface between $LiNiO_2$ (104) surface and amorphous Co_xB conducted longer-time AIMD simulations at 2500 K for 12.0 ps. Projected density of states and schematic local environment (insets of b-d) of (b) lattice oxygen coordinated by 3 Ni and 3 Li, (c) interface oxygen coordinated by 1 Co, 2 Ni and 3 Li, and (d) interface oxygen coordinated by 1 B, 2 Ni and 2 Ni.

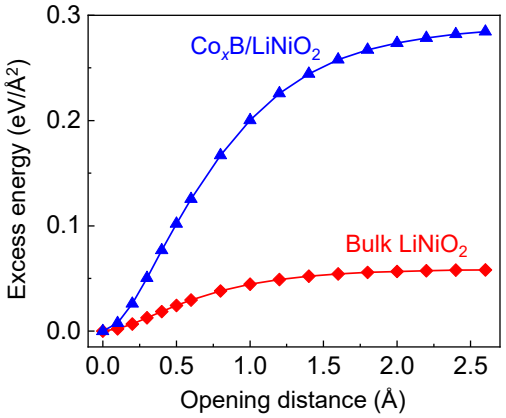

Supplementary Figure 32 | Excess energy as a function of opening distance at $Co_xB/LiNiO_2$ interface between amorphous Co_xB and $LiNiO_2$ (104) slab and at (104) face of bulk $LiNiO_2$. For $Co_xB/LiNiO_2$ interface, the same relaxed structure as **Fig. 6** (a supercell containing 20 Li, 20 Ni, 40 O, 35 Co and 16 B) was used and the "opening" was chosen at the lower $Co_xB/LiNiO_2$ interface. The Brillouin zone was sampled using Monhorst-Pack scheme with a 2×3×2 **k**-point mesh. For bulk $LiNiO_2$, a relaxed supercell cell containing 32 Li, 32 Ni, and 64 O was used and cut to expose two (104) surfaces. The Brillouin zone was sampled using Monhorst-Pack scheme with a 2×2×2 **k**-point mesh. No ionic relaxations were performed when calculating the excess energy.

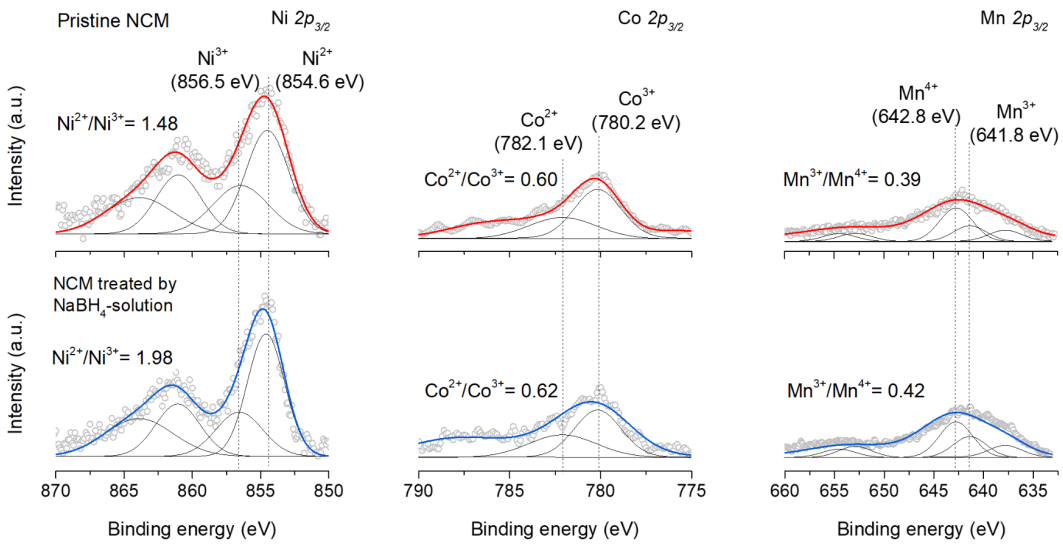

Supplementary Figure 33 | XPS data of Ni $2p_{3/2}$, Co $2p_{3/2}$, and Mn $2p_{3/2}$ for (upper panel) pristine NCM and (lower panel) NCM treated by ethanol solution containing 0.156 M $NaBH_4$ for 2 h at room temperature.

Supplementary Table 1 | Chemical composition of Co_xB-NCM and pristine NCM measured by ICP-OES.

Sample	Mole ratio over (Ni+Co+Mn) (%)					Weight percentage (mg g^{-1})	
	Li	Ni	Co	Mn	B	Co	B
Co_xB-NCM	101.8	79.447	10.683	9.837	0.033	68.526	0.121
Pristine NCM	102.0	79.549	10.505	9.945	/	67.097	/

Supplementary Table 2 | Refined XRD data for Co_xB-NCM and pristine NCM.

Co_xB-NCM	Element	Site	*x*	*y*	*z*	Occupancy
a=2.87250(3) Å *c*=14.18805(6) Å R_{wp} = 10.26% R_p = 7.25% *S* = 1.781	Li	3a	0	0	0	0.989(7)
	Li	3b	0	0	0.5	0.011(7)
	Co	3b	0	0	0.5	0.108(4)
	Ni	3b	0	0	0.5	0.783(4)
	Mn	3b	0	0	0.5	0.098(4)
	Ni	3a	0	0	0	0.011(6)
	O	6c	0	0	0.259722	1.0(4)

Pristine NCM	Element	Site	*x*	*y*	*z*	Occupancy
a=2.87273(3) Å *c*=14.18885(5) Å R_{wp} = 10.44% R_p = 7.12% *S* = 1.865	Li	3a	0	0	0	0.988(7)
	Li	3b	0	0	0.5	0.012(8)
	Co	3b	0	0	0.5	0.106(4)
	Ni	3b	0	0	0.5	0.783(3)
	Mn	3b	0	0	0.5	0.099(6)
	Ni	3a	0	0	0	0.012(6)
	O	6c	0	0	0.259643	1.0(4)

Supplementary Table 3 | Particle size distributions of Co_xB-NCM and pristine NCM.

Sample	Particle size distribution		
	D_{10} (μm)	D_{50} (μm)	D_{90} (μm)
Co_xB-NCM	5.4	11.9	16.2
Pristine NCM	5.8	12.4	16.2

Supplementary Table 4 | XPS binding energies with attributed species and curve fitting results for Co_xB-NCM and pristine NCM in **Fig. 2g-n**.

Spectra details	Binding energy (eV)	Attributed species	FWHM (eV)		Reference
			Co_xB-NCM	Pristine NCM	
B 1*s*	187.8	B in Co_xB	1.1	/	[R1, R2]
Co 2*p*	778.5	Metallic-like Co in Co_xB (blue)	1.8	/	[R3]
	780.2	Co^{3+} (red)	2.0	1.9	[R4, R5]
	782.1	Co^{2+} (violet)	2.0	2.0	
Ni $2p_{3/2}$	854.6	Ni^{2+} (red)	/	1.8	
	856.5	Ni^{3+} (orange)	/	2.2	
	861.0	Ni^{2+} (yellow)	/	2.2	
	863.9	Ni^{3+} (violet)	/	2.8	
Ni $2p_{1/2}$	872.3	Ni^{2+} (sky blue)	/	2.0	
	874.0	Ni^{3+} (blue)	/	2.6	
	879.2	Ni^{2+} (black)	/	2.8	
Mn $2p_{3/2}$	641.8	Mn^{3+} (orange)	/	4.0	
	642.8	Mn^{4+} (yellow)	/	3.6	
Mn $2p_{1/2}$	653.2	Mn^{3+} (violet)	/	4.4	
	654.4	Mn^{4+} (sky blue)	/	4.2	

*The shoulder peak at 637.5 eV is related with Auger peak.

**The area ratio of ($2p_{1/2}$ to $2p_{3/2}$) in pristine NCM: 1.997 for Co; 2.005 for Ni; 1.987 for Mn.

Supplementary Table 5 | Major components of cathode electrode and electrolyte interphases (CEIs) generated during electrochemical cycling and corresponding curve fitting results for Co_xB-NCM and pristine NCM after cycling in **Fig. 4g-k** for the present study.

Component	Chemical species of interest	Details
Polyvinylidene fluoride (PVDF) binder	$–CF_2$	The peaks of $–CF_2$ in C 1s (291.0 eV) and F 1s (688.1 eV) implies the presence of polyvinylidene fluoride binder in cathode electrode [R6].
Decomposition products of $LiPF_6$	LiF_2, NiF_2, $Li_xPO_yF_z$	Commonly observed in electrolyte with fluorinated salt such as $LiPF_6$. Metal fluorides, including LiF and NiF_2 (685.2 eV in F 1s, 857.1 and 875.2 eV in Ni 2p), can be generated from reactions among active materials, semicarbonates and HF produced by hydrolysis of PF_6^-. The $Li_xPO_yF_z$ signal (686.1 eV in F 1s) also confirms the decomposition of LiPF6 [R6].
Polycarbonate	CH_2^-, C_2HO^-, CH_3O^-, $(CH_2CH_2OCOO)_n$	The possible route for formation of polycarbonates could be the oxidative polymerization of cyclic carbonates (e.g. ethylene carbonate) in electrolyte[R7,R8]. The C 1s peaks characteristics of C–O (286.5 eV) and C=O (289.5, 291.2 eV) are indicators of poly(ethylene carbonate, PEC) formation[R9,R10]. The peak of C–C (284.9 eV) could be ascribed to the decomposition products of carbonate-based electrolyte as well.
$ROCO_2Li$, Li_2CO_3	CH_2^-, C_2HO^-, CH_2O^-, CO_3, C=O	Semicarbonates (lithium alkyl carbonate and lithium carbonate) are generally generated in carbonate containing electrolyte, such as ethylene, diethyl, or dimethyl carbonates. The C 1s peaks characteristics of C–O (CH_2O, 286.5 eV) and C=O (CO_3, 289.5 eV) are related to lithium carbonate/lithium alkyl carbonate[R11].

Supplementary Table 6 | Concentration of dissolved Ni, Co and Mn in electrolytes measured by ICP-OES, for Co_xB-NCM and pristine NCM cells after certain cycles during 7 C-discharge cycling at 45 °C. For each measurement, electrolytes from three cells were measured to calculate the average and standard deviation.

Sample	Co_xB-NCM/Li cell			Pristine NCM/Li cell		
	Ni (ppm)	Co (ppm)	Mn (ppm)	Ni (ppm)	Co (ppm)	Mn (ppm)
100 cycles	12.14±4.77	3.22±0.03	4.38±0.05	122.82±3 .11	11.22±0.55	24.3±0.67
200 cycles	77.26±6.67	9.31±0.74	14.73±3.45	477.82±22.5	33.87±5.88	67.88±10.67

Supplementary Table 7 | Water content in pristine NCM and Co_xB-NCM.

Sample	Pristine NCM	Co_xB-NCM
Water content (ppm)	234.6 ± 20.5	256.1 ± 13.3

Supplementary Table 8 | Impurity contents of LiOH and Li_2CO_3 in pristine NCM and Co_xB-NCM.

Sample	Pristine NCM		Co_xB-NCM	
Impurity contents (ppm)	LiOH	Li_2CO_3	LiOH	Li_2CO_3
	1770 ± 160	3800 ± 130	1880 ± 220	3450 ± 110

Supplementary Table 9 | Full-cell specifications. (CC: constant current. CV: constant voltage.)

Full-cell specifications		
	Cathode	Anode
Sample	Pristine NCM / Co_xB-NCM	Spherical graphite (Gr)
Cell dimension	72.5 mm*54 mm	75.5 mm*58mm
Composition	Active material (AM) : CM : Bi = 93 : 3.5 : 3.5 (CM: carbon black, Bi: polyvinylidene fluoride, PVDF)	AM : CMC : SBR = 97.5 : 1.1 : 1.4 (CMC: carboxymethyl cellulose, SBR: styrene butadiene rubber)
One-side Loading level (mg cm^{-2})	13.5 ± 0.1	8.2 ± 0.1
Two-side Loading level (mg cm^{-2})	27.1 ± 0.2	16.4 ± 0.2
Electrode thickness (μm)	95 ± 1 (Al foil thickness of 15μm included)	123 ± 1 (Cu foil thickness of 10μm included)
Electrode density (g cm^{-3})	3.35 ± 0.02	1.44 ± 0.02
Stacking	2	3
Negative/positive (N/P) ratio	1.11 ± 0.01	
Separator thickness (μm)	10	
Amount of electrolyte	1.0 g (~2.5g Ah^{-1})	
Formation step testing condition	Voltage range: 2.8 – 4.30 V Charge: 0.1C (CC) – 0.05C (CV) / Discharge: 0.1C (CC) Charge/discharge current density: 0.27 mA cm^{-2}	
Cycling test condition	Voltage range: 2.8 – 4.30 V Charge: 1.0C (CC) – 0.05C (CV) / Discharge: 1.0C (CC) Charge/discharge current density: 2.70 mA cm^{-2}	

Supplementary References

[R1] Masa, J. et al. Amorphous Cobalt Boride (Co_2B) as a Highly Efficient Nonprecious Catalyst for Electrochemical Water Splitting: Oxygen and Hydrogen Evolution. *Adv. Energy Mater.* **6**, 1502313 (2016).

[R2] Jiang, B. et al. A mesoporous non-precious metal boride system: synthesis of mesoporous cobalt boride by strictly controlled chemical reduction. *Chem. Sci.* **11**, 791-796 (2020).

[R3] Deng, J. et al. Co–B Nanoflakes as Multifunctional Bridges in $ZnCo_2O_4$ Micro-/Nanospheres for Superior Lithium Storage with Boosted Kinetics and Stability. *Adv. Energy Mater.* **9**, 1803612 (2019).

[R4] Zhang, C. et al. Revealing the role of NH_4VO_3 treatment in Ni-rich cathode materials with improved electrochemical performance for rechargeable lithium-ion batteries. *Nanoscale* **10**, 8820-8831 (2018).

[R5] Chen, Z. et al. Hierarchical Porous $LiNi_{1/3}Co_{1/3}Mn_{1/3}O_2$ Nano-/Micro Spherical Cathode Material: Minimized Cation Mixing and Improved Li^+ Mobility for Enhanced Electrochemical Performance. *Sci. Rep.* **6**, 25771 (2016).

[R6] Zhao, W. et al. High Voltage Operation of Ni-Rich NMC Cathodes Enabled by Stable Electrode/Electrolyte Interphases. *Adv. Energy Mater.* **8**, 1800297 (2018).

[R7] M. Gauthier et al. Electrode–Electrolyte Interface in Li-Ion Batteries: Current Understanding and New Insights. *J. Phys. Chem. Lett.* **6**, 22, 4653–4672 (2015).

[R8] I. Shkrob et al. Reduction of Carbonate Electrolytes and the Formation of Solid-Electrolyte Interface (SEI) in Lithium-Ion Batteries. 1. Spectroscopic Observations of Radical Intermediates Generated in One-Electron Reduction of Carbonates. *J. Phys. Chem. C* **117**, 38, 19255–19269 (2013).

[R9] Zheng, J., Engelhard, M., Mei, D. et al. Electrolyte additive enabled fast charging and stable cycling lithium metal batteries. *Nat. Energy* **2**, 17012 (2017).

[R10] Li Yang et al. Electrolyte Reactions with the Surface of High Voltage $LiNi_{0.5}Mn_{1.5}O_4$ Cathodes for Lithium-Ion Batteries. *Electrochem. Solid-State Lett.* **13**(8), A95-A97 (2010).

[R11] Zheng, J. et al. Highly Stable Operation of Lithium Metal Batteries Enabled by the Formation of a Transient High-Concentration Electrolyte Layer. *Adv. Energy Mater.* **6**, 1502151 (2016).